Journal of Advanced Ceramics
2024, **13**(11): 1807–1822
https://doi.org/10.26599/JAC.2024.9220978

Research Article

A systematic study of thermomechanical properties and calcium–magnesium–aluminosilicate (CMAS) corrosion of multicomponent rare-earth phosphates

Keith Bryce[1], Bishnu Pada Majee[1,2], Liping Huang[2], Jie Lian[1,2,✉]

[1] *Department of Mechanical, Aerospace and Nuclear Engineering, Rensselaer Polytechnic Institute, NY 12180, USA*
[2] *Department of Materials Science & Engineering, Rensselaer Polytechnic Institute, NY 12180, USA*

Received: June 14, 2024; Revised: September 23, 2024; Accepted: September 25, 2024

Abstract: Multicomponent rare earth phosphates hold immense potential as next-generation environmental barrier coatings (EBCs), offering enormous possibilities and flexibility by controlling and varying their components and fractions to tailor their performance. In this work, the key material parameters (e.g., ionic size and ionic size disorder) and the elements governing their thermal–mechanical properties and resistance against calcium–magnesium–aluminosilicate (CMAS) corrosion were elucidated. The thermal conductivities of multicomponent rare-earth phosphates correlate well with cation size disorder, but no clear trend is identified for the coefficient of thermal expansion (CTE). Er-containing compositions display low CTEs and high fracture toughness. Rapid formation of a dense interfacial layer occurs for most CAMS corrosion-resistant compositions when tested at 1300 °C, e.g., $(Lu_{0.2}Yb_{0.2}Er_{0.2}Y_{0.2}Gd_{0.2})PO_4$ and $(Lu_{0.2}Yb_{0.2}Er_{0.2}Dy_{0.2}Gd_{0.2})PO_4$. These multicomponent phosphates also display the least recession upon molten CMAS attack at 1400 °C without significant volumetric swelling, which is superior to their single-component counterparts and state-of-the-art EBCs based on rare-earth disilicates. In contrast, Sc-containing multicomponent phosphates display inferior performance against CMAS corrosion and penetration. A mechanistic understanding and understanding of the kinetics of the interfacial interaction at higher temperatures, as well as the key parameters governing their thermomechanical properties and CMAS corrosion, are valuable for designing data-driven materials of multicomponent phosphates for EBC applications.

Keywords: environmental barrier coating (EBC); high-entropy ceramics (HECs); rare earth phosphates; calcium−magnesium−aluminosilicate (CMAS); corrosion; thermal properties; ytterbium disilicate

1 Introduction

SiC-based ceramic matrix composites (CMCs) are widely used as jet engine components throughout the aerospace industry because of their high mechanical strength and lightweight properties compared with those of metal alloys [1]. However, these CMC components need to perform at temperatures above 1500 °C, where they experience active oxidation in environments containing water vapor and calcium-magnesium-aluminosilicate (CMAS) corrosion at high temperatures. Hence, they must be coated with environmental barrier coatings (EBCs) to prevent degradation. EBCs must be chemically compatible with the SiC substrate, have a closely matched coefficient of thermal expansion (CTE) with the substrate, not undergo phase changes at elevated temperatures, and be chemically resistant to water vapor and molten CMAS [2].

High-entropy ceramics (HECs), known as multicomponent ceramics, are attracting considerable attention within the materials community because of their promising characteristics, which arise from a range of beneficial effects. One such characteristic is their enhanced mechanical properties, such as increased hardness and yield strength [3]. This enhancement is attributed to the lattice distortions caused by the mixture of cations with different ionic radii, which create barriers that impede the propagation of dislocations, thereby obstructing plastic deformation [4]. HECs also have increased thermal stability as atomic mobility is reduced because of the crystal lattice strain, and at high temperatures, reduced atomic mobility helps maintain the structural integrity of the material, preventing grain growth and phase transformations that can degrade thermal stability [5]. Another property of HECs is their improved corrosion resistance due to their sluggish diffusion mechanism, where atoms must move through a highly distorted and energetically complex lattice; this mechanism inherently slows the inward and outward diffusion of ions [6]. This sluggish diffusion mechanism also leads to reduced grain growth, as reduced atomic mobility limits the coarsening of grains, resulting in a finer microstructure [4].

For EBC applications, the increased chemical durability of HECs is of particular interest, as high-temperature CMAS and water vapor corrosion are two common failure modes for EBCs [7]. Several multicomponent ceramics have been suggested for EBC applications. In particular, rare earth disintegrates, owing to their close CTE matching with SiC as well as their high thermal stability, are the current state-of-the-art EBCs, and several multicomponent disilicate compositions have been synthesized and tested [8]. Recently, Xiao *et al.* [9] synthesized and tested the

✉ Corresponding author.
E-mail: lianj@rpi.edu

清華大学出版社 Tsinghua University Press | SciOpen

CMAS corrosion resistance of multicomponent rare earth disilicates ($(Y_{0.25}Sc_{0.25}Er_{0.25}–Yb_{0.25})_2Si_2O_7$, $(Y_{0.2}Sc_{0.2}Er_{0.2}Yb_{0.2}Lu_{0.2})_2Si_2O_7$, and $(Y_{0.2}Sc_{0.2}Er_{0.2}Yb_{0.2}Gd_{0.2})_2–Si_2O_7$)) and reported that at 1300 °C for 48 h, maximizing lattice distortion contributed to improved CMAS corrosion resistance. However, disilicates with smaller average cation ionic radii presented better CMAS corrosion resistance at 1500 °C. However, Wei *et al.* [10] synthesized and examined the CMAS corrosion of $(Yb_{0.2}Y_{0.2}Lu_{0.2}Ho_{0.2}Er_{0.2})_2Si_2O_7$, $(Yb_{0.2}Y_{0.2}Lu_{0.2}Sc_{0.2}Gd_{0.2})_2Si_2O_7$, $(Yb_{0.2}Tm_{0.2}Lu_{0.2}Sc_{0.2}Gd_{0.2})_2Si_2O_7$, and $(Yb_{0.2}Tm_{0.2}Lu_{0.2}Sc_{0.2}Er_{0.2})_2Si_2O_7$ at 1300 °C for 48 h and reported reduced CMAS penetration depths with increased average cation radii, with all four samples showing improved CMAS corrosion resistance compared with $Yb_2Si_2O_7$. In addition, single-phase $(Y_{0.25}Yb_{0.25}Er_{0.25}Sc_{0.25})_2Si_2O_7$, $(Dy_{0.25}Ho_{0.25}Tm_{0.25}Yb_{0.25})_2Si_2O_7$, and $(Lu_{0.125}Yb_{0.125}Sc_{0.125}Er_{0.125}Y_{0.125}Ho_{0.125}Dy_{0.125}Tb_{0.125})_2Si_2O_7$ have also been synthesized and reported to display improved CMAS corrosion resistance compared with single-component disilicates [11–13].

Multicomponent rare earth monosilicates have also been proposed for EBC applications. Fan *et al.* [14] compared the CMAS corrosion resistance of $(Lu_{0.25}Yb_{0.25}Er_{0.25}Y_{0.25})_2SiO_5$ and $(Lu_{0.2}Yb_{0.2}Er_{0.2}Ho_{0.2}Y_{0.2})_2SiO_5$ to Y_2SiO_5 plasma-sprayed coatings and reported that multicomponent monosilicate exhibited better corrosion resistance than Y_2SiO_5 due to the increased formation of a garnet phase, which limited the further penetration of CMAS into the monosilicate coatings. Ren *et al.* [15] successfully synthesized single-phase $(Y_{0.25}Ho_{0.25}Er_{0.25}Yb_{0.25})_2SiO_5$, which showed a lower thermal conductivity and CTE than estimations based on the mixing rule. Other types of multicomponent ceramics have also been suggested for EBC applications. Zhao *et al.* [16] proposed the use of $(Y_{0.2}Nd_{0.2}Sm_{0.2}Eu_{0.2}Er_{0.2})AlO_3$ to replace $YAlO_3$ as part of a trilayer EBC system $REAlO_3$/$RE_3Al_5O_{12}$/(Al_2O_3/Al_2O_3 CMCs) because of its reduction in thermal conductivity.

Rare earth phosphates, particularly the xenotime phase, constitute another group of ceramics that have recently been investigated for potential EBC applications because of their high melting points, phase stability at elevated temperatures, comparable CTEs to rare earth disilicates, chemical compatibility with SiO_2 (oxidation product of SiC substrate), and improved CMAS corrosion resistance compared with rare earth silicates [17,18]. Zhang *et al.* [19] and Zhang *et al.* [20] synthesized xenotime phase $(Dy_{0.166}Ho_{0.166}Er_{0.166}Tm_{0.166}Yb_{0.166}Y_{0.166})PO_4$ and $(Ho_{0.143}Tm_{0.143}Yb_{0.143}Lu_{0.143}Dy_{0.143}Er_{0.143}Y_{0.143})PO_4$, respectively, which both showed reduced thermal conductivity compared with single-component phosphates, excellent thermal stability up to 1750 °C, and little to no reaction with SiO_2 at 1400 °C after 5 h [19,20]. Bryce *et al.* [21] synthesized and tested $(Lu_{0.2}Yb_{0.2}Er_{0.2}Y_{0.2}Gd_{0.2})PO_4$, which has a lower thermal conductivity than single-component xenotime phosphates and comparable CMAS corrosion resistance to that of $LuPO_4$ tested by Hu *et al.* [17]. Multicomponent monazite-phase rare earth phosphates such as $(La_{0.2}Ce_{0.2}Nd_{0.2}Sm_{0.2}Eu_{0.2})PO_4$ and $(La_{0.143}Ce_{0.143}Pr_{0.143}Nd_{0.143}Sm_{0.143}Eu_{0.143}Gd_{0.143})PO_4$ have also been investigated as potential thermal barrier coatings (TBCs) due to their phase stability, close CTE match with that of Al_2O_3, good chemical compatibility with Al_2O_3 at high temperatures, and lower thermal conductivity than single-component monazite-phase rare earth phosphates [22,23]. While these multicomponent rare earth phosphate compositions improve the thermal and chemical properties compared with those of single-component phosphates, many other possible multicomponent rare phosphates can be synthesized while maintaining the single-phase xenotime structure necessary for EBC applications.

The specific contributions of rare earth elements (REEs) to the thermomechanical properties and CMAS corrosion resistance of multicomponent phosphates remain largely unknown, as does the direct comparison of these properties with those of single-component phosphates in the context of EBC applications. There has also been no direct comparison of CMAS corrosion resistance of these multicomponent phosphates to that of current state-of-the-art EBCs such as $Yb_2Si_2O_7$. Therefore, we carried out a systematic study using cation size disorder as a descriptor for predicting the CMAS corrosion resistance and thermomechanical properties of multicomponent rare earth phosphates. The five multicomponent rare earth phosphates investigated in the study are listed in Table 1, where the degree of cation size disorder is calculated via Eq. (1) [24]. The compositions were selected to ensure that at least five elements occupied the principal cation sublattice, with as wide a range of cation size disorders as possible while maintaining the single-phase xenotime structure.

$$\delta = \sqrt{\sum_{i=0}^{n} x_i \left(1 - \frac{r_i}{r_{\text{avg}}}\right)^2} \quad (1)$$

where x_i is the atomic percentage, r_{avg} is the average cation radius, r_i is the radius of the ith species, and n is the number of rare earth species.

2 Materials and methods

The single and multicomponent rare earth phosphate powders used in this study were synthesized via the chemical coprecipitation method outlined in Ref. [21]. After synthesis, the powders were dried at 90 °C for 12 h, crushed into fine powders via a mortar and pestle, and then calcined at 1000 °C for 12 h. $Yb_2Si_2O_7$ used for a comparative study was synthesized via solid-state reactions using Yb_2O_3 and SiO_2 as precursor materials. The mixture of precursor powders was milled via a high-energy ball mill (FRITSCH-pulverisette 7, Fritsch GmbH, Germany) with ethanol as the mixing solvent and ZrO_2 milling balls as the grinding materials. The powders were milled at 500 r·min^{-1} for 40 cycles of 30 min with 10 min pause in between cycles, after

Table 1 List of xenotime structure multicomponent rare-earth phosphates with their average cation radius, cation size disorder, measured pellet density, theoretical density, and pellet porosity

Compound	Average cation radius (pm)	Cation size disorder, δ (%)	Measured density (g·cm^{-3})	Theoretical density (g·cm^{-3})	Porosity (%)
$(Lu_{0.2}Yb_{0.2}Er_{0.2}Y_{0.2}Gd_{0.2})PO_4$	100.76	2.68	5.83±0.02	6.00	2.83
$(Sc_{0.1}Lu_{0.3}Yb_{0.3}Er_{0.2}Y_{0.1})PO_4$	97.83	3.94	5.82±0.02	6.06	3.96
$(Sc_{0.1}Lu_{0.3}Yb_{0.2}Y_{0.3}Gd_{0.1})PO_4$	98.81	4.68	5.49±0.03	5.61	2.14
$(Sc_{0.2}Lu_{0.2}Yb_{0.2}Y_{0.2}Gd_{0.2})PO_4$	98.08	6.28	5.33±0.05	5.53	3.62
$(Sc_{0.2}Lu_{0.2}Yb_{0.2}Y_{0.2}Sm_{0.2})PO_4$	98.60	6.92	5.19±0.02	5.46	4.95

which the slurry was dried at 90 °C for 12 h and then calcined at 1000 °C for 12 h. The phase compositions of all the calcined powders were confirmed via an X-ray diffractometer (XRD; Panalytical X'Pert Pro system; Westborough, USA) with a copper target (K_α = 0.15406 nm) and a step size of 0.013°, where K_α is the characteristic X-ray emission from the copper anode.

$REPO_4$ pellets were fabricated by loading approximately 1–1.2 g of finely ground calcined powders into 10 mm diameter cylindrical graphite dies and sintering them into dense pellets via a spark plasma sintering (SPS) system (Model 10-3 SPS system, Thermal Tech. LLC, USA) under a steady flow of argon gas (1 L·min^{-1}). All the $REPO_4$ pellets were sintered at 1500 °C and 50 MPa for 5–30 min, depending on the composition of the $REPO_4$, whereas the $Yb_2Si_2O_7$ pellets were sintered at 1500 °C and 50 MPa for 15 min. The pellets were heated and cooled at a rate of 200 °C·min^{-1}. Next, the pellets were ground with SiC abrasive papers and then polished with 0.06 μm silica colloidal paste on an appropriate polishing cloth to achieve a mirror finish.

CTEs of rectangular $REPO_4$ coupons (10 mm × 8 mm × 2 mm) were determined via a thermal dilatometer (DIL; 402 Expedis Supreme, NETZCH, Germany), where the pellets were heated from room temperature to 1300 °C at a heating rate of 10 °C·min^{-1}. The density of the pellets was measured using the Archimedes technique on an Adam analytical scale (AE Adam, Adam Equipment, UK) with deionized water as the immersion medium. A laser flash apparatus (LFA; LFA-457, NETZCH, Germany) was used to measure the thermal diffusivity of $REPO_4$ pellets that were 1.2–1.8 mm thick. Before LFA measurement, both sides of a pellet were polished to a mirror finish and uniformly coated with spray graphite paste to improve laser energy absorption and emissivity. The samples were heated at a rate of 5 °C·min^{-1}, at which the thermal diffusivity of the samples was evaluated via the Cape–Lehmann method on the basis of a nonlinear regression model from 27–1000 °C. The specific heat capacities (c_p) of the multicomponent rare earth phosphates were estimated by applying the Neumann–Kopp rule of mixtures using the constituent single-component rare-earth phosphates according to their chemical compositions [25–29]. The thermal conductivity, k (W·m^{-1}·K^{-1}), was calculated via Eq. (2), where ρ is the density of the sample pellet and α is the thermal diffusivity (mm^2·s^{-1}).

$$k = \alpha \rho c_P \tag{2}$$

$$k_{\text{measured}} = k(1-P)^{1.5} \tag{3}$$

The thermal conductivity was also corrected to be a fully dense and pure phase to eliminate the effects of porosity via Eq. (3) [30] and the Neumann–Kopp mixture rule for a fully dense and pure phase pellet to eliminate the effects of porosity. Equation (3) shows the formula for the corrected thermal conductivity (k_{measured}), where P is the porosity of the measured pellet. The elastic modulus and hardness of the as-sintered pellets were measured via nanoindentation at room temperature via a triboindenter (Hysitron TI900, Bruker, USA) equipped with a diamond Berkovich tip with a three-sided pyramid shape. A linear pattern of indents was generated via instrument automation software with an indent spacing of 15 μm, with a load function of a ramp rate of 200 μN·s^{-1} to a peak load of 1000 μN for 12 s, followed by unloading at the same constant rate to zero load. More than 20 indentations were generated for every sample. Fracture toughness was determined via a microhardness tester (Leco M-400, LECO Corporation, USA). At least 10 indentations were generated for each sample with a load of 1 kgF (~9.8 N), and each indentation lasted for 15 s. The average crack length of each indentation was measured from the corresponding scanning electron microscopy (SEM) images from the crack tips following the cracking path for each indentation.

The CMAS composition used in this investigation is 33CaO–9MgO–13$AlO_{1.5}$–45SiO_2, a commonly studied composition [18,31,32], with CaO (99.99%; Sigma-Aldrich, Germany), MgO (99.99%; Sigma-Aldrich, Germany), Al_2O_3 (99.99%; Sigma-Aldrich, Germany), and SiO_2 (99.9%; Alfa Aesar, USA) used as the starting materials. The precursor powders were combined in a Pt crucible according to their stoichiometric ratios, heated to 1500 °C for 8 h at a heating rate of 10 °C·min^{-1}, and then quenched in water to produce CMAS glass. The CMAS glass was then ground to create uniform granularity, and approximately 60 mg·cm^{-2} (for reactions at 1300 °C) or 40 mg·cm^{-2} (for reactions at 1400 °C) of this CMAS was placed at the center of the polished top surface of the $REPO_4$ pellet, heated in a box furnace (Carbolite HFT 1800, Carbolite Gero, UK) at a rate of 10 °C·min^{-1} in air and cooled at a rate of 10 °C·min^{-1}. The phase compositions of the CMAS-embedded samples were confirmed via XRD. After testing, the samples were mounted in epoxy, cut in half to reveal the sample cross sections, and then polished to a mirror finish before SEM analysis. An SEM (SUPRA 55, Zeiss, Germany) equipped with an energy-dispersive X-ray spectroscopy (EDS) detector was used to analyze the microstructure at the sample cross-section, and EDS mapping and line scanning for elemental analysis were performed.

3 Results and discussion

3.1 Phase and thermomechanical properties of multicomponent rare-earth phosphates

XRD patterns of the rare-earth phosphates synthesized via the coprecipitation method are shown in Fig. 1, where all the compositions display a xenotime structure with no apparent secondary phases. In a study by Bryce *et al.* [21], $(Lu_{0.2}Yb_{0.2}Er_{0.2}Y_{0.2}Gd_{0.2})PO_4$ was synthesized, with Gd^{3+} being the largest rare-earth ion successfully incorporated in the xenotime phase. However, by incorporating 20 mol% Sc^{3+} (the smallest rare-earth ion) in the cation sublattice, it is also possible to include up to 20 mol% larger lanthanides, such as Sm^{3+}, in the mixture while still maintaining the xenotime phase. This was also attempted with both 10 and 20 mol% Nd^{3+}; however, Nd^{3+} was never fully incorporated into the xenotime phase, and a monazite impurity phase was observed in the mixture. The lattice parameter of each multicomponent rare earth phosphate was calculated through peak refinement via the MDI Jade 6.5 software and plotted against the average ionic radius of the principal cations in Fig. 1(b). The figure shows a general increase in the lattice parameters with increasing average ionic radius. This trend is typically observed in multicomponent metal oxides, where larger cations at the A-site, such as Gd and Sm, lead to greater lattice expansion [33]. The trend is also observed at the highlighted (200) reflection, where a shift to a lower angle coincides with an increased average ionic radius.

Figure 2(a) shows the thermal conductivity of the multicomponent rare earth phosphates from room temperature to 1273 K. The thermal conductivity is corrected for a fully dense material, as porosity can significantly impede heat transfer and reduce a material's thermal conductivity. The results show a reduction in thermal conductivity with increasing temperature due to the increased scattering of lattice vibrations, which is expected for most ceramics [34]. Compared with single-

component phosphates such as $LuPO_4$ and YPO_4, all multicomponent samples present reduced thermal conductivity [21]. Among the five multicomponent compositions synthesized, $(Sc_{0.2}Lu_{0.2}Yb_{0.2}Y_{0.2}Sm_{0.2})PO_4$ displays the lowest thermal conductivity (2.04 $W{\cdot}m^{-1}{\cdot}K^{-1}$) at room temperature. Figure 2(b) shows the plot of thermal conductivity at room temperature vs. cation size disorder, and a clear trend can be identified in the reduction in thermal conductivity with increased cation size disorder. This demonstrates that the increased lattice distortion of HECs results in reduced thermal conductivity; thus, cation size disorder can serve as a predictive parameter for the thermal conductivity of high-entropy rare earth phosphates. This finding may facilitate the development of predictive models for thermal properties.

Figure 3 displays the temperature dependence of the linear CTEs for the multicomponent phosphate samples from 500 to 1573 K. The 5 compositions studied $(Lu_{0.2}Yb_{0.2}Er_{0.2}Y_{0.2}Gd_{0.2})PO_4$ and $(Sc_{0.1}Lu_{0.3}Yb_{0.3}Er_{0.2}Y_{0.1})PO_4$ have the lowest CTEs, which vary from 4.6×10 to 6.8×10^{-6} K^{-1}, whereas $(Sc_{0.2}Lu_{0.2}Yb_{0.2}Y_{0.2}Gd_{0.2})PO_4$ has the highest CTE, which varies from 5.0×10^{-6} to 7.1×10^{-6} K^{-1} over the observed temperature range. The $(Sc_{0.2}Lu_{0.2}Yb_{0.2}Y_{0.2}Gd_{0.2})PO_4$ sample also shows a slight decrease in CTE above 1500 K. Since the xenotime phase does not undergo a phase transformation, this decrease in CTE could be due to the diffusion of point defects, such as vacancies, at increased temperatures. This diffusion alters the volume and thermal expansivity of the crystals [35]. There is no clear trend in CTE with respect to the average ionic radius or cation size disorder, but $ErPO_4$ has the lowest CTE of all the single-component phosphates, and the two compositions with Er have the lowest CTE [36].

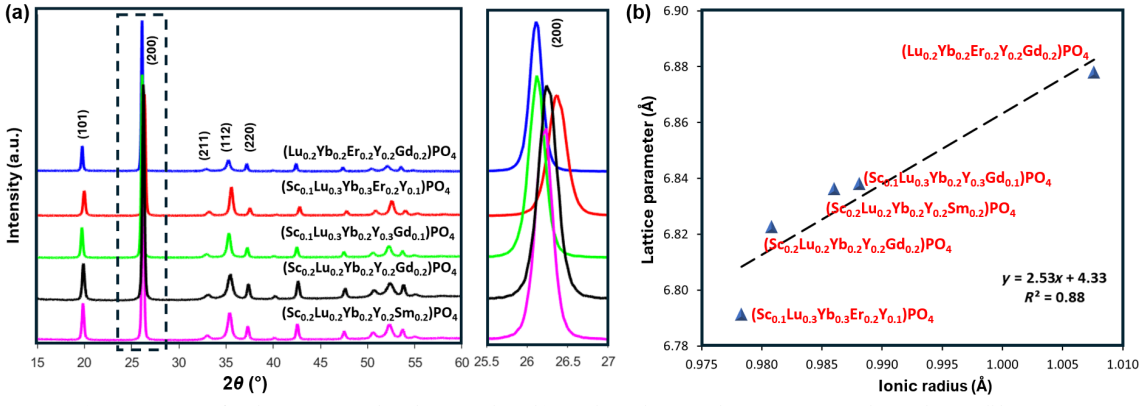

Fig. 1 (a) XRD patterns of multicomponent phosphate powders; (b) correlation between the average ionic radius and unit cell lattice parameter.

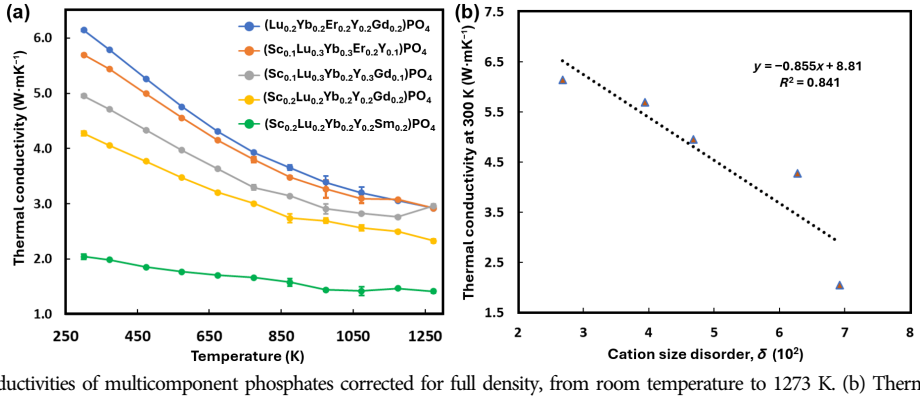

Fig. 2 (a) Thermal conductivities of multicomponent phosphates corrected for full density, from room temperature to 1273 K. (b) Thermal conductivity at room temperature vs. cation size disorder of each multicomponent phosphate.

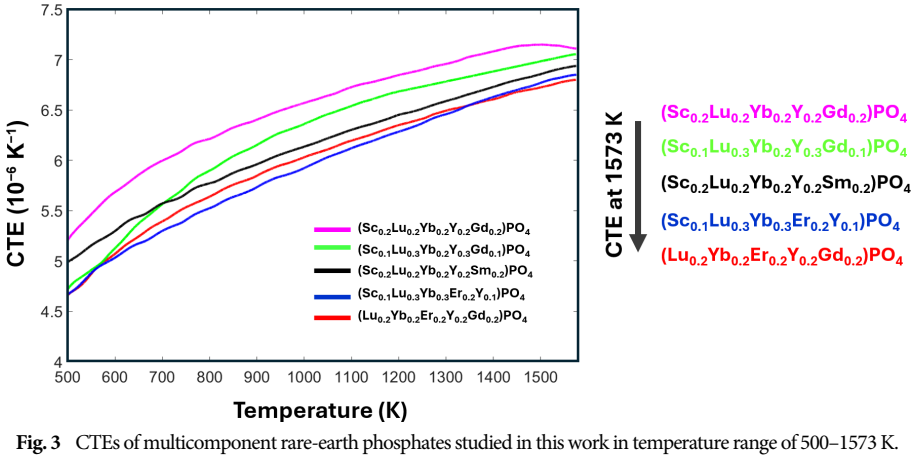

Fig. 3 CTEs of multicomponent rare-earth phosphates studied in this work in temperature range of 500–1573 K.

Figure 4(a) displays the measured elastic modulus of the multicomponent rare earth phosphates, where $(Sc_{0.2}Lu_{0.2}Yb_{0.2}Y_{0.2}Gd_{0.2})PO_4$ has the highest elastic modulus of 184.4 GPa and $(Lu_{0.2}Yb_{0.2}Er_{0.2}Y_{0.2}Gd_{0.2})PO_4$ has the lowest value of 154.9 GPa. The elastic modulus is a measure of the stiffness of a material and is heavily dependent on the bond strength. In ceramics, stronger bonds typically result in a higher elastic modulus. If the lattice parameter increases due to weaker bonding, the elastic modulus should decrease. This trend is somewhat apparent in Fig. 4(c), which shows a slight negative correlation between the elastic modulus and the lattice constant of the multicomponent phosphates. However, since the elastic modulus depends on other factors, such as the crystal structure and microstructure, the lattice parameter, and, consequently, the bond strength alone cannot accurately predict the bulk elastic modulus of new multicomponent phosphates. Notably, $(Lu_{0.2}Yb_{0.2}Er_{0.2}Y_{0.2}Gd_{0.2})PO_4$ has a significantly lower elastic modulus than the other samples do, and it is the only sample that does not contain Sc. Additionally, the two samples with 20 mol% Sc have the highest elastic modulus. In a study by Han *et al.* [36], where the shear modulus (G) and bulk modulus (B) of $ScPO_4$, $LuPO_4$, $YbPO_4$, $ErPO_4$, and YPO_4 were calculated, they reported that the B/G ratios of $REPO_4$ except for $ScPO_4$ were in the range of 1.99–2.11, where B/G ratios above 2.0 indicate excellent ductility. However, $ScPO_4$ has a B/G value of 1.66, indicating that it is more brittle than the other rare earth phosphates. This might explain why the samples with the most Sc have the highest elastic modulus. Similar to the elastic modulus, the measured hardness values show no clear trends with respect to the average ionic radius or the degree of cation size disorder. $(Sc_{0.1}Lu_{0.3}Yb_{0.2}Y_{0.3}Gd_{0.1})PO_4$ and $(Sc_{0.2}Lu_{0.2}Yb_{0.2}Y_{0.2}Gd_{0.2})PO_4$ have the highest hardness values of 12.5 and 12.6 GPa, respectively, whereas $(Lu_{0.2}Yb_{0.2}Er_{0.2}Y_{0.2}Gd_{0.2})PO_4$ has the lowest value of 10.3 GPa. Han *et al.* [36] calculated the hardness values of single-component rare earth phosphates to be between 8.24 and 11.29 GPa. In our work, the hardness of multicomponent phosphates ranged from 10.3 to 12.6 GPa, indicating a similar level of resistance against plastic deformation. Another mechanical property of note is the shear modulus, which measures a material's ability to resist shear deformation and indicates its stiffness under shear stress. Like hardness, the shear modulus depends on the bond strength and atomic arrangement of the material. Figure 4(d) shows a plot of the shear modulus (G) vs. the lattice parameter of the multicomponent phosphates, where $G = E/2(1+\nu)$, E is the elastic modulus, and ν is the Poisson's ratio. Poisson's ratio was approximated via the mixing rule and the calculated Poisson's ratios of single-component phosphates from a study by Han *et al.* [36]. The plot shows a weak negative correlation between the shear modulus and the lattice parameter. A negative correlation would be expected since larger lattice parameters would coincide with weaker bonds, making the material less resistant to deformation.

Figure 5(a) shows the measured fracture toughness of the multicomponent rare earth phosphates, with $(Lu_{0.2}Yb_{0.2}Er_{0.2}Y_{0.2}Gd_{0.2})PO_4$ having the highest toughness of 1.6±0.2 MPa·m$^{1/2}$, indicating that it is the most fracture resistant among the multicomponent rare earth phosphates investigated in this study. The fracture toughness of $(Lu_{0.2}Yb_{0.2}Er_{0.2}Y_{0.2}Gd_{0.2})PO_4$ is also comparable to that of other studied EBC candidates, such as $Yb_2Si_2O_7$ (2.0 MPa·m$^{1/2}$) and $Y_2Si_2O_7$ (2.12 MPa·m$^{1/2}$) [37]. The index of brittleness β is a parameter proposed by Lawn *et al.* [38] and measures the degree of competition between deformation and fracture. $\beta = H/K_{IC}$ where H is the hardness, K_{IC} is the fracture toughness and is used to compare the brittleness of different materials, with the more brittle material having higher β values. Figure 5(b) shows a plot of the index of brittleness vs. the lattice

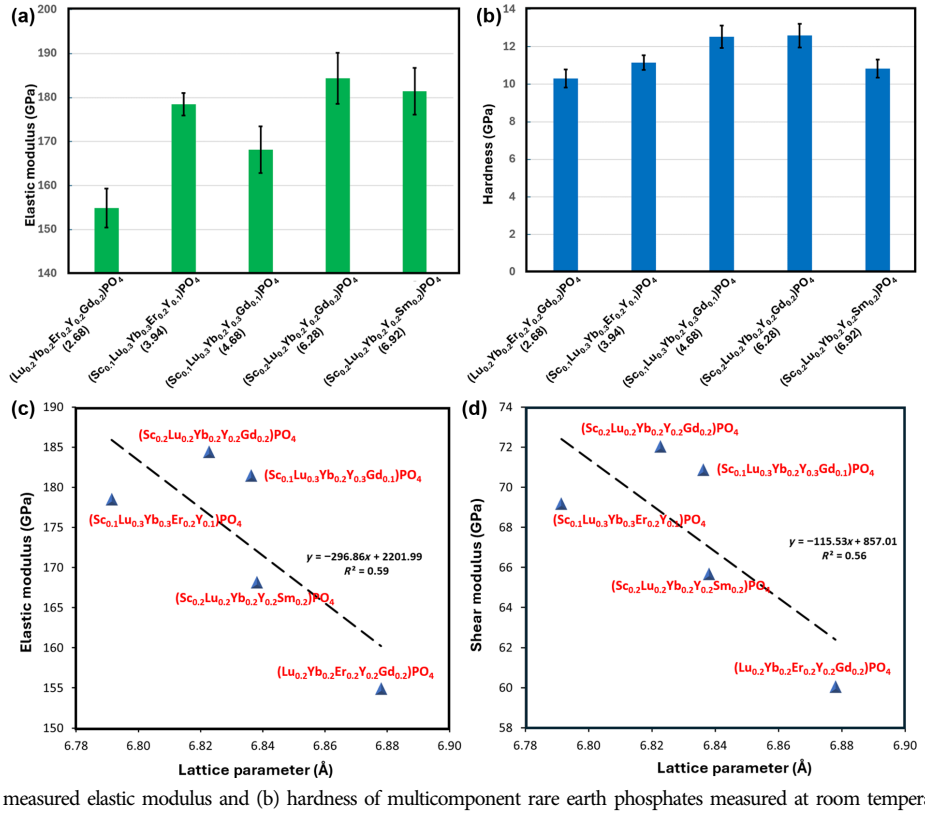

Fig. 4 Summary of (a) measured elastic modulus and (b) hardness of multicomponent rare earth phosphates measured at room temperature. Plots of (c) elastic modulus and (d) shear modulus vs. lattice parameter of each multicomponent rare earth phosphate.

parameter, where $(Lu_{0.2}Yb_{0.2}Er_{0.2}Y_{0.2}Gd_{0.2})PO_4$ has the lowest index of brittleness, confirming that it is the most damage tolerant of the multicomponent phosphates studied; however, it has a greater index of brittleness than more state-of-the-art EBC candidates, such as $Yb_2Si_2O_7$ (3.4 $\mu m^{-1/2}$) and $Y_2Si_2O_7$ (2.92 $\mu m^{-1/2}$) [37]. Overall, similar to those of single-component phosphates, the mechanical properties of multicomponent phosphates are not well correlated with material properties such as ionic radii and lattice parameters. Therefore, successful predictions of the mechanical properties of the many possible compositions of multicomponent phosphates will need to encompass computational modeling in tandem with experimental testing.

3.2 CMAS exposure of multicomponent rare-earth phosphates at 1300 °C

Figure S1 in the Electronic Supplementary Material (ESM) shows XRD patterns taken at the surface layer of $(Lu_{0.2}Yb_{0.2}Er_{0.2}Y_{0.2}Gd_{0.2})PO_4$ pellets with CMAS deposits after heat treatment at 1300 °C for 96 h, while XRD patterns for the remaining 4 samples are shown in Figs. S2–S5 in the ESM. The diffraction peaks for all 5 samples were indexed, and the bulk material $REPO_4$ along with the $Ca_8MgRE(PO_4)_7$ and $RE_2Si_2O_7$ phases were observed in all of the XRD patterns, with the closest matching single component versions of the phases used to index the diffraction peaks. In the study by Bryce *et al.* [21] using a CMAS composition of $40CaO–5MgO–5AlO_{1.5}–50SiO_2$, a $Ca_2RE_8(SiO_4)_6O_2$ secondary phase was observed in the residual CMAS after reaction with $(Lu_{0.2}Yb_{0.2}Er_{0.2}Y_{0.2}Gd_{0.2})PO_4$ at 1300 °C for 45 h. However, this $Ca_2RE_8(SiO_4)_6O_2$ phase was not observed in this study; instead, a $RE_2Si_2O_7$ secondary phase was observed. This is likely due to the difference in CMAS compositions between the two reactions. A reaction with CMAS containing more Ca increases the likelihood of precipitating phases with higher Ca contents, such as $Ca_2RE_8(SiO_4)_6O_2$. In contrast, if there is less Ca available in CMAS melt, phases with no Ca, such as $RE_2Si_2O_7$, are more likely to precipitate. $RE_2Si_2O_7$ diffraction peaks are the most intense in all of the samples except for $(Lu_{0.2}Yb_{0.2}Er_{0.2}Y_{0.2}Gd_{0.2})PO_4$. However, it is unclear whether this is due to a lower quantity of disilicate precipitate in this reaction or the result of the specific location where XRD characterization was performed.

SEM backscattered electron images at the interface of $(Lu_{0.2}Yb_{0.2}Er_{0.2}Y_{0.2}Gd_{0.2})PO_4$–CMAS reaction at 1300 °C for 96 h are displayed in Fig. 6. A uniform and dense layer consisting of multiple phases can be observed in the SEM images, and the

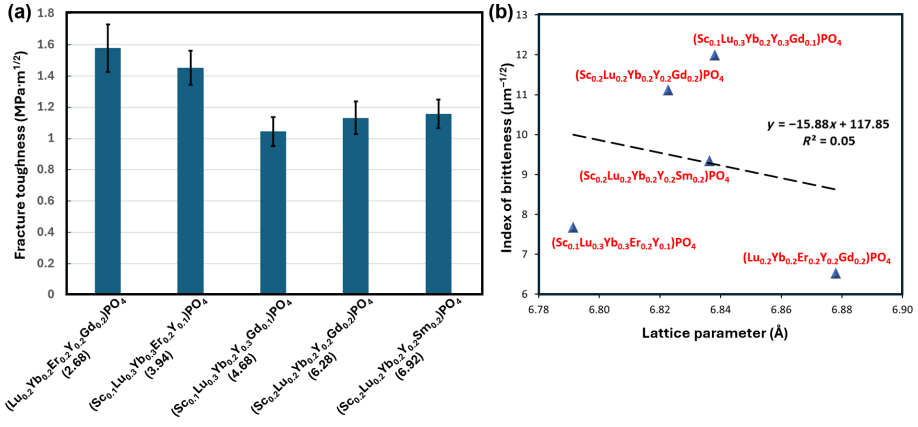

Fig. 5 (a) Indentation fracture toughness of the multicomponent rare earth phosphates measured at room temperature and (b) plot of index of brittleness vs. lattice parameter of each multicomponent phosphate.

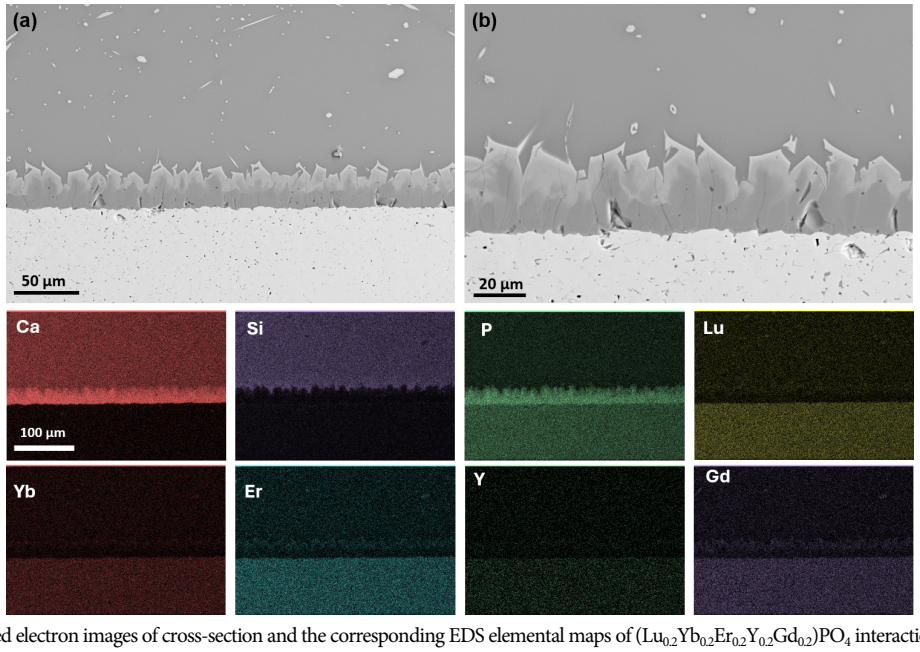

Fig. 6 SEM backscattered electron images of cross-section and the corresponding EDS elemental maps of $(Lu_{0.2}Yb_{0.2}Er_{0.2}Y_{0.2}Gd_{0.2})PO_4$ interaction with molten CMAS at 1300 °C for 96 h: (a) low- and (b) high-magnification images of reaction layer.

thickness of the reaction layer is estimated to be 29.4±2.0 μm. The pores below the reaction layer were generally free of CMAS, with little Ca signal observed below the reaction layer, indicating that the reaction layer was effective in halting CMAS penetration into the bulk pellet. Minor precipitates are observed in the residual CMAS. On the basis of the diffraction measurements, the lighter contrasts are likely $RE_2Si_2O_7$ precipitates. EDS elemental maps clearly show the enrichment of REEs in the top section of the reaction layer, with Ca and P being enriched in the bottom section, indicating a variation in stoichiometry along the depth of the reaction layer.

SEM backscattered electron images of $(Sc_{0.1}Lu_{0.3}Yb_{0.3}Er_{0.2}Y_{0.1})PO_4$ pellet along the cross-section after CMAS corrosion at 1300 °C for 96 h are displayed in Fig. 7. SEM images show the residual CMAS layer and the bulk pellet separated by a uniform and dense reaction layer that is approximately 33.4±4.8 μm thick, with little to no CMAS penetrating below the reaction layer. There is also minor delamination of the reaction layer from the bulk pellet, as indicated by the small crack between them, possibly caused by mechanical polishing before SEM analysis. Large, lighter contrast precipitates are observed in the residual CMAS, which are confirmed to be $RE_2Si_2O_7$ precipitates on the basis of EDS and XRD analysis. There appears to be less variation in the contrast between the top and bottom sections of the reaction layer, and the EDS maps do not show clear enrichment of Lu, Yb, and Er at the top of the reaction layer. However, Sc appears to be more enriched in the reaction layer than within the bulk pellet, suggesting preferential incorporation of Sc into the interfacial reaction layer.

Figure 8 presents SEM backscattered electron images of

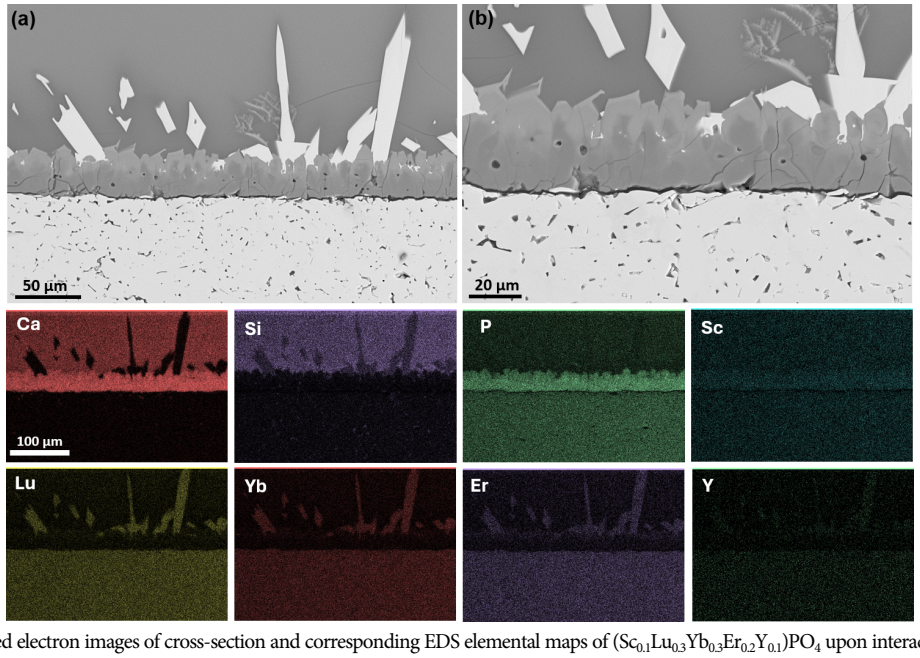

Fig. 7 SEM backscattered electron images of cross-section and corresponding EDS elemental maps of $(Sc_{0.1}Lu_{0.3}Yb_{0.3}Er_{0.2}Y_{0.1})PO_4$ upon interaction with molten CMAS at 1300 °C for 96 h: (a) low- and (b) high-magnification images of reaction layer.

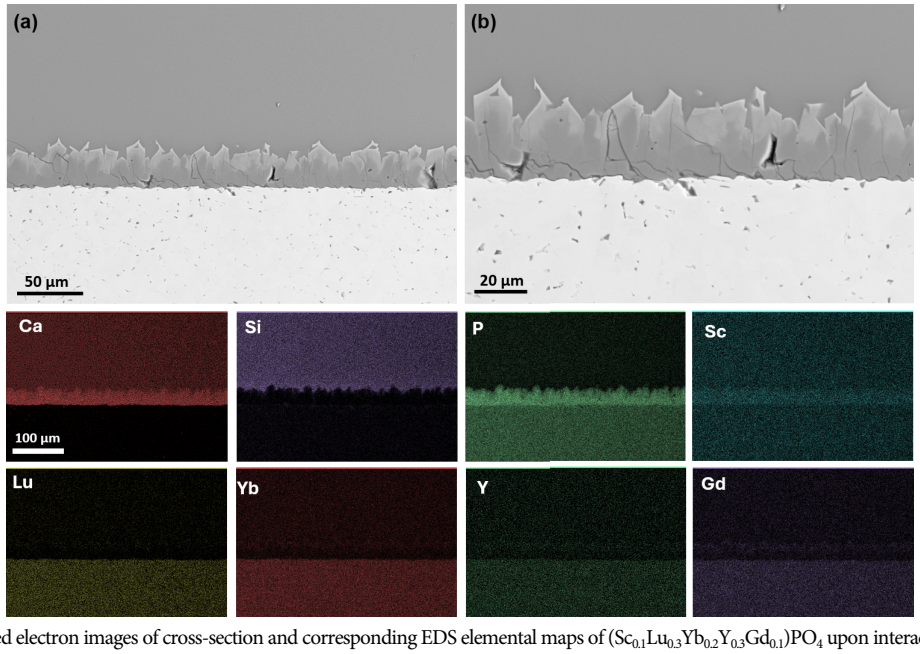

Fig. 8 SEM backscattered electron images of cross-section and corresponding EDS elemental maps of $(Sc_{0.1}Lu_{0.3}Yb_{0.2}Y_{0.3}Gd_{0.1})PO_4$ upon interaction with molten CMAS at 1300 °C for 96 h: (a) low- and (b) high-magnification images of reaction layer.

$(Sc_{0.1}Lu_{0.3}Yb_{0.2}Y_{0.3}Gd_{0.1})PO_4$ after CMAS corrosion at 1300 °C for 96 h. A uniform reaction layer is formed between CMAS and $(Sc_{0.1}Lu_{0.3}Yb_{0.2}Y_{0.3}Gd_{0.1})PO_4$ pellet, which is approximately 29.6±2.8 μm thick with little CMAS penetrating below the reaction layer. EDS maps again suggest a compositional variation in the REEs along the depth of the reaction layer, with Yb, Y, and Gd concentrated toward the top of the reaction layer. However, Sc appears uniform throughout the reaction layer and is even more enriched than it is within the bulk pellet.

Figure 9 shows SEM backscattered electron images of $(Sc_{0.2}Lu_{0.2}Yb_{0.2}Y_{0.2}Gd_{0.2})PO_4$–CMAS interface after the reaction at 1300 °C for 96 h. The multilevel reaction layer is 35.0±3.2 μm thick, with Lu, Yb, Y, and Gd enriched at the top portion of the layer. The light contrast precipitate within the residual CMAS is enriched in REEs and Si and is likely the $RE_2Si_2O_7$ phase. Overall, little to no CMAS is observed between the grains below the reaction layer.

SEM backscattered electron images of $(Sc_{0.2}Lu_{0.2}Yb_{0.2}Y_{0.2}Sm_{0.2})PO_4$ pellet cross-section after CMAS corrosion at 1300 °C for 96 h are displayed in Fig. 10. SEM images show that the residual CMAS layer and the bulk pellet are separated by a uniform and dense reaction layer that is approximately 37.9±3.5 μm thick, with little CMAS penetrating below the reaction layer. Large, brighter contrast precipitates are also observed in the residual CMAS enriched with Sc, Lu, and Yb and are likely $RE_2Si_2O_7$ precipitates. Again, REEs appear to be enriched at the top position of the reaction, particularly Sm.

In summary, the reaction mechanism between all the multicomponent phosphates and CMAS at 1300 °C proceeds via the dissolution of $REPO_4$ into the molten CMAS, and once the

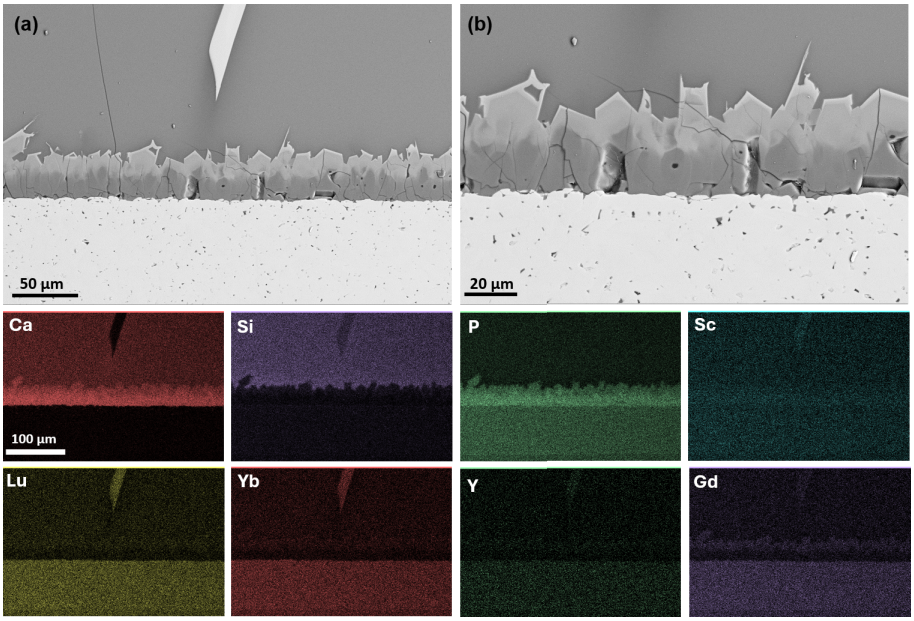

Fig. 9 SEM backscattered electron images of cross-section and corresponding EDS elemental maps of $(Sc_{0.2}Lu_{0.2}Yb_{0.2}Y_{0.2}Gd_{0.2})PO_4$ upon interaction with molten CMAS at 1300 °C for 96 h: (a) low- and (b) high-magnification images of reaction layer.

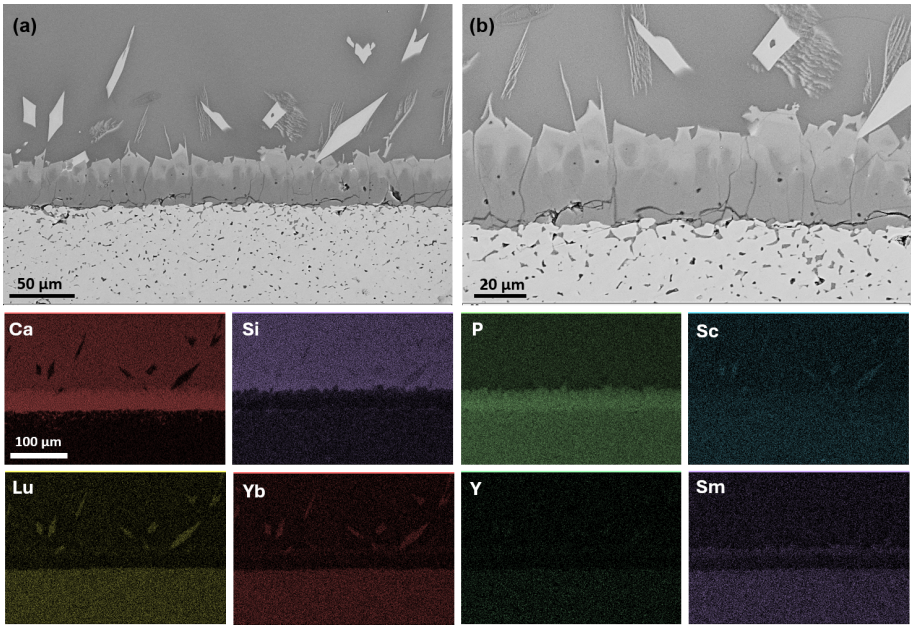

Fig. 10 SEM backscattered electron images of cross-section and corresponding EDS elemental maps of $(Sc_{0.2}Lu_{0.2}Yb_{0.2}Y_{0.2}Sm_{0.2})PO_4$ upon interaction with molten CMAS at 1300 °C for 96 h: (a) low- and (b) high-magnification images of reaction layer.

concentrations of rare elements and phosphorus within the melt reach a saturation state, $Ca_8MgRE(PO_4)_7$ begins to precipitate at the interface between the melt and the bulk pellet. At this point, the molten CMAS must diffuse through the reaction layer to reach the bulk pellet, significantly reducing the rate at which the bulk material is consumed by CMAS melt. As the thickness of the reaction layer increases, the overall rate of the dissolution-diffusion reaction decreases [21]. Additionally, a rare earth disilicate phase precipitates in the residual melt once the concentration of REEs within CMAS melt reaches a saturation state, and Ca : Si ratio decreases to an equilibrium point because of Ca uptake caused by the formation of $Ca_8MgRE(PO_4)_7$ phase. This reprecipitation phenomenon is also observed during CMAS reaction of multicomponent rare earth disintegrates at 1500 °C for 25 h [39]. There is an observable variation in the contrast of the reaction layer for all five samples. This likely results from the formation of a nonstoichiometric $(Ca_{2+x}RE_{8-x}(PO_4)_x(SiO_4)_{6-x}O_2)$ version of $Ca_8MgRE(PO_4)_7$, where Ca^{2+} and PO_4^{3-} ions are partially substituted by RE^{3+} and SiO_4^{4-} ions.

Figures 11(a)–11(c) show an EDS line scan along the depth of the reaction layer formed at the interface between $(Sc_{0.2}Lu_{0.2}Yb_{0.2}Y_{0.2}Gd_{0.2})PO_4$ pellet and CMAS. As shown in Fig. 11(b), Ca and P are clearly enriched in the reaction layer closer to the bulk pellet and decrease in concentration closer to the top of the reaction layer, whereas Si and the REE(s) appear to be more concentrated toward the top of the reaction layer and decrease in concentration toward the bulk pellet. However, REE(s) do not all have the same variation along the depth of the reaction layer, as Fig. 11(c) shows that the concentration of Sc increases toward the bulk pellet, opposite to that of Lu, Yb, Y, and Gd. This could mean that Sc is reprecipitating in $Ca_8MgRE(PO_4)_7$ phase at a higher rate than the other REE(s) because its smaller ionic size means Sc can be easily incorporated into the interfacial layer. For comparison, an EDS line scan of $(Lu_{0.2}Yb_{0.2}Er_{0.2}Y_{0.2}Gd_{0.2})PO_4$–CMAS reaction layer was performed, and the results are displayed in Fig. 11(d). Similar to $(Sc_{0.2}Lu_{0.2}Yb_{0.2}Y_{0.2}Gd_{0.2})PO_4$ pellet, there is an enrichment of Ca and P closer to the bulk pellet, whereas REE(s) are more concentrated toward the top of the reaction layer, as shown in Fig. 11(e). However, Fig. 11(f) shows that all REE(s) follow the same general trend of being enriched at the top of the reaction layer and depleted near the bottom of the reaction layer.

The above results show that $REPO_4$–CMAS reaction at 1300 °C proceeded via a dissolution reprecipitation reaction. Hence, the rate at which the bulk material dissolves in the CMAS directly affects the rate at which $Ca_8MgRE(PO_4)_7$ precipitates at the interface, and a thicker reaction layer indicates that $REPO_4$ is more reactive with the CMAS melt [40]. Here, we compare the reaction layer thickness of each multicomponent phosphate with measurements from a study by Majee *et al.* [41], where CMAS interaction behaviors with single-component $ScPO_4$, $LuPO_4$, $YbPO_4$, $ErPO_4$, and YPO_4 were investigated after exposure at 1300 °C for 96 h with the same $33CaO–9MgO–13AlO_{1.5}–45SiO_2$ CMAS. Figure 12 displays the reaction layer thickness of single and multicomponent phosphates after CMAS reaction at 1300 °C for 96 h. The multicomponent phosphates all have thinner reaction layers than all the reported single-component phosphates do, indicating their improved resistance against CMAS corrosion at 1300 °C. The initial stage of $REPO_4$–CMAS reaction is dominated by the dissolution of $REPO_4$ phase into CMAS melt. Once $Ca_8MgRE(PO_4)_7$ phase begins to precipitate and a dense layer forms, the reaction rate becomes more dependent on the rate

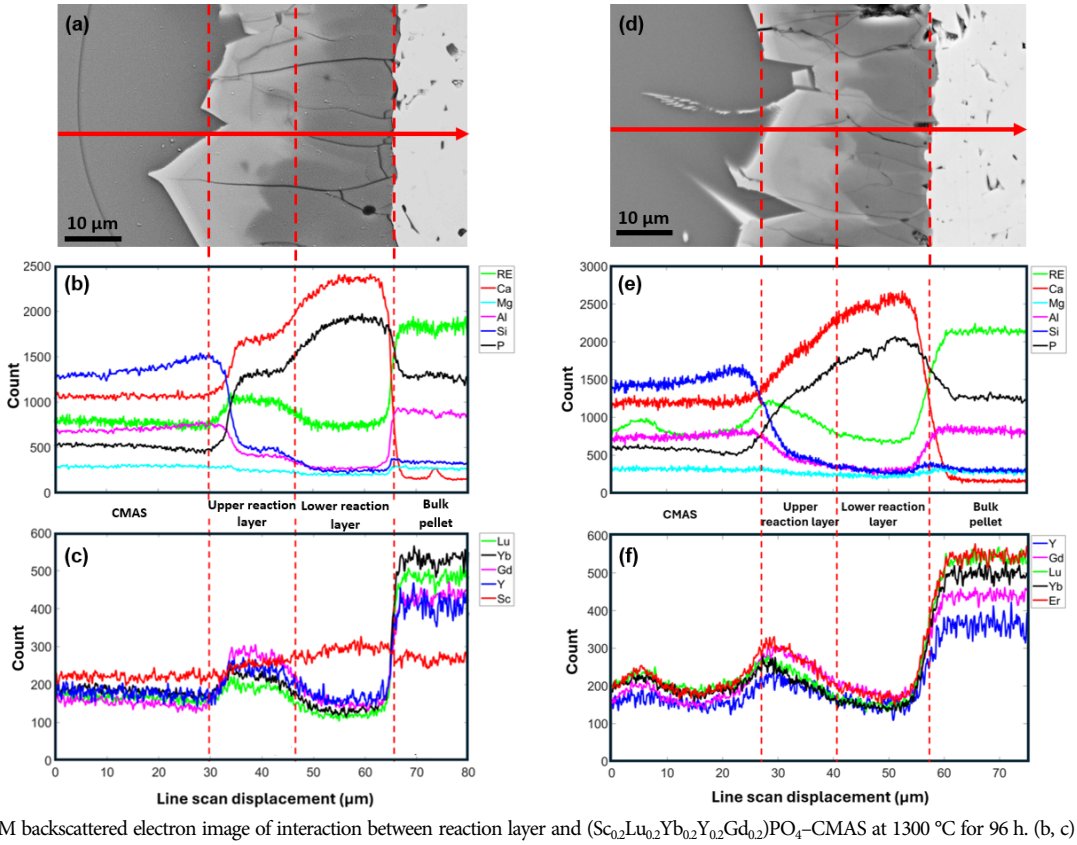

Fig. 11 (a) SEM backscattered electron image of interaction between reaction layer and $(Sc_{0.2}Lu_{0.2}Yb_{0.2}Y_{0.2}Gd_{0.2})PO_4$–CMAS at 1300 °C for 96 h. (b, c) EDS line plots along the red line indicated in (a). (d) SEM backscattered electron image of interaction between reaction layer and $(Lu_{0.2}Yb_{0.2}Er_{0.2}Y_{0.2}Gd_{0.2})PO_4$–CMAS at 1300 °C for 96 h. (e, f) Plots of EDS line scans indicated in (d).

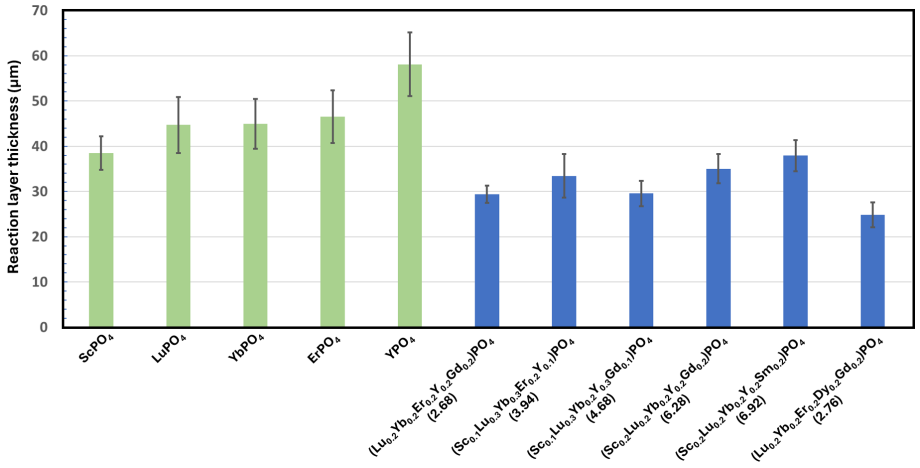

Fig. 12 Measured reaction layer thickness of single-component and multicomponent phosphates after reaction with molten CMAS at 1300 °C for 96 h. The single-component measurements are taken from Majee *et al.* [41].

at which CMAS and $REPO_4$ ions diffuse across $Ca_8MgRE(PO_4)_7$ interface. The distorted lattice structure of the multicomponent $Ca_8MgRE(PO_4)_7$ phase creates a more tortuous and complex path for the inward and outward diffusion of ions. This distorted lattice structure likely impedes the diffusion of CMAS ions across the interface more effectively than the regular lattice structure of single-component phosphates [42]. Consequently, the rate at which CMAS interacts with $REPO_4$ is reduced, thereby decreasing the overall reaction rate. Notably, the multicomponent samples containing the highest content of Sc, such as $(Sc_{0.2}Lu_{0.2}Yb_{0.2}Y_{0.2.2})PO_4$ and $(Sc_{0.2}Lu_{0.2}Yb_{0.2}Y_{0.2}Sm_{0.2})PO_4$), have thicker reaction layers than the samples with less or no Sc (i.e., $(Lu_{0.2}Yb_{0.2}Er_{0.2}Y_{0.2}Gd_{0.2})PO_4$)), and considering that Sc shows a different variation across the depth of the reaction layer than the other REE(s) in Fig. 11(c), it appears to cause an increase in the reaction layer thickness. CMAS corrosion of $ScPO_4$ was investigated by Majee *et al.* [41], who reported that $ScPO_4$ has the thinnest reaction layer of all single-component phosphates, likely because Sc^{3+} has the smallest ionic radius of the other REEs, which corresponds to it having the highest RE–O bond strength and making it the most stable rare earth phosphate. Hence, the inclusion of Sc in the multicomponent structure should increase the CMAS corrosion resistance from a rule-of-mixture perspective, but it appears to have the opposite effect.

To test whether Sc had a negative effect on the $REPO_4$–CMAS interaction, a sixth multicomponent phosphate $(Lu_{0.2}Yb_{0.2}Er_{0.2}Dy_{0.2}Gd_{0.2})PO_4$ was synthesized using only lanthanide elements and tested under the same conditions as the initial five multicomponent phosphates. Figure S6 in the ESM shows XRD patterns taken at the surface layer of the $(Lu_{0.2}Yb_{0.2}Er_{0.2}Dy_{0.2}Gd_{0.2})PO_4$ pellets with CMAS deposits after heat treatment at 1300 °C for 96 h. The diffraction peaks were indexed, and $Ca_8MgRE(PO_4)_7$ was the only phase observed, which was indexed by the structural characteristics of $Ca_8MgGd(PO_4)_7$ (PDF#50-1766), as it is the closest matching single component version of $Ca_8MgRE(PO_4)_7$. Notably, no $RE_2Si_2O_7$ diffraction peaks were observed. This could be due to Ca:Si ratio of CMAS melt being too high (> 3.1) for $RE_2Si_2O_7$ phase to precipitate, as the increased corrosion resistance of $(Lu_{0.2}Yb_{0.2}Er_{0.2}Dy_{0.2}Gd_{0.2})PO_4$ composition means that less Ca is consumed from CMAS melt [43].

SEM backscattered electron images of $(Lu_{0.2}Yb_{0.2}Er_{0.2}Dy_{0.2}Gd_{0.2})PO_4$ pellet along the cross-section after CMAS corrosion at 1300 °C for 96 h are displayed in Fig. 13. The images show the residual CMAS layer and the bulk pellet is separated by a uniform and dense reaction layer, with little CMAS penetrating below the reaction layer. No bright contrast precipitates are observed in the residual CMAS, which agrees with the lack of $RE_2Si_2O_7$ peaks in XRD analysis. This confirms that no $RE_2Si_2O_7$ precipitates formed during the reaction. There is a clear variation in the contrast between the top and bottom sections of the reaction layer, and EDS maps clearly reveal enrichment of all REE(s) at the top of the reaction layer. Figure 14 shows a higher magnification image of $(Lu_{0.2}Yb_{0.2}Er_{0.2}Dy_{0.2}Gd_{0.2})PO_4$ pellet reaction layer and EDS line scans. Ca and P are enriched closer to the bulk pellet, similar to other multicomponent phosphates, whereas all REE(s) are more concentrated toward the top of the reaction layer, as illustrated in Figs. 14(b) and 14(c). The reaction layer thickness is approximately 24.8±2.7 μm, showing a decrease in the reaction layer thickness from $(Lu_{0.2}Yb_{0.2}Er_{0.2}Y_{0.2}Gd_{0.2})PO_4$ sample, making $(Lu_{0.2}Yb_{0.2}Er_{0.2}Dy_{0.2}Gd_{0.2})PO_4$ the most CMAS-resistant multicomponent phosphate tested.

CMAS corrosion of different multicomponent phosphates was compared and correlated with their structural characteristics to identify the underlying mechanisms and the key material parameters/structural characteristics governing their performance. The reaction layer thickness of single-component rare earth phosphates following their interaction with molten CMAS has been shown to decrease with decreasing REE ionic radius up to Lu. This reduction could be attributed to the smaller ionic size of lanthanides and stronger metal-oxygen bonds, which reduce the dissolution of the phosphate in CMAS melt and improve their corrosion resistance. However, for the multicomponent phosphates, there is a weaker trend in the opposite direction between the average ionic radii of REE cations and their reaction layer thickness, as shown in Fig. 15(a). Here, the reaction layer thickness increases with decreasing REE ionic radius due to the inclusion of smaller Sc^{3+} ions in compositions with smaller average ionic radii, which appears to negatively affect CMAS corrosion resistance of rare earth phosphates. However, an increase in cation size disorder seems to have a negative effect on the corrosion resistance of rare earth phosphates, as Fig. 15(b) shows a slightly positive trend between the reaction layer thickness and REE ionic radius size disorder. This is also likely due to the inclusion of Sc in the compositions. Sc, which is smaller in size, significantly increases the degree of cation size disorder. Since Sc appears to negatively affect CMAS corrosion resistance when included in a multicomponent mixture, samples with greater cation size disorder will contain more Sc and consequently exhibit

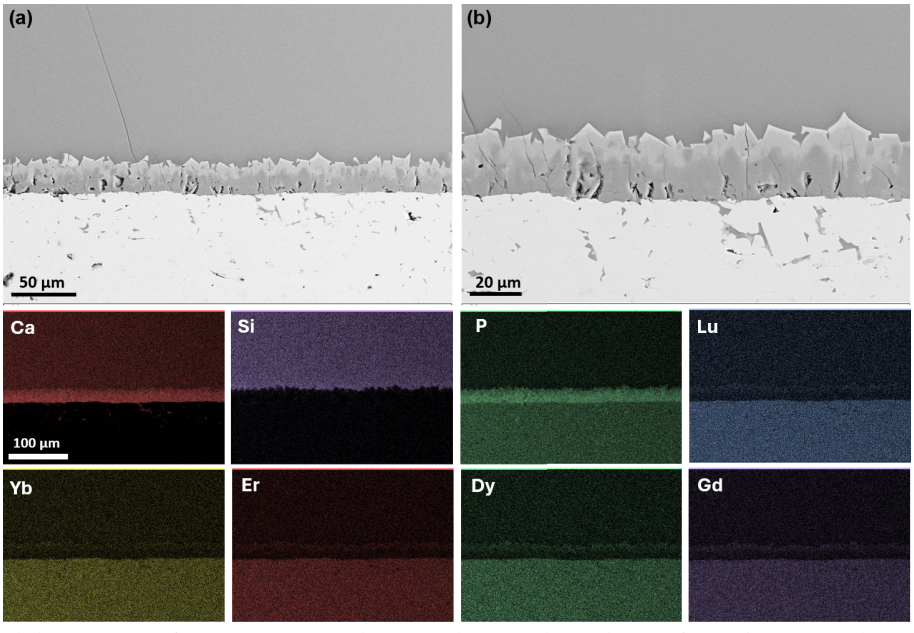

Fig. 13 SEM backscattered electron images of cross-section view and corresponding EDS elemental maps of $(Lu_{0.2}Yb_{0.2}Er_{0.2}Dy_{0.2}Gd_{0.2})PO_4$ interaction with molten CMAS at 1300 °C for 96 h: (a) low- and (b) high-magnification images of reaction layer.

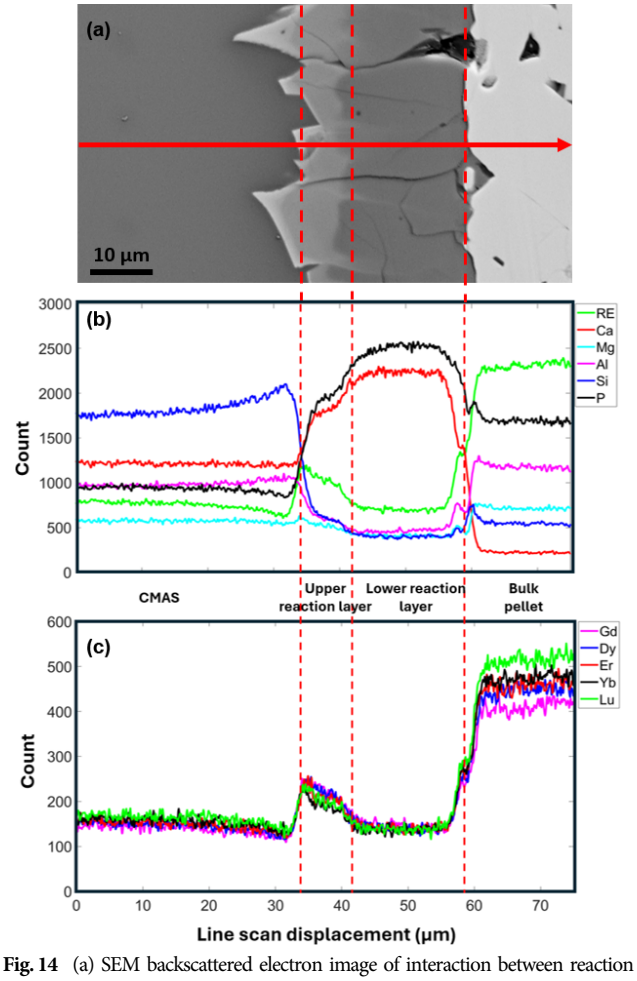

Fig. 14 (a) SEM backscattered electron image of interaction between reaction layer and $(Lu_{0.2}Yb_{0.2}Er_{0.2}Dy_{0.2}Gd_{0.2})PO_4$–CMAS at 1300 °C for 96 h. (b, c) Plots of EDS line scan indicated in (a).

lower CMAS resistance. Overall, neither correlation appears to be very strong. Therefore, other factors, such as the performance of the individual constituents, must also be considered when designing a multicomponent phosphate.

It has been speculated that rare earth phosphates may display better resistance against CMAS corrosion than state-of-the-art rare earth disilicates do on the basis of comparisons between different studies of both materials [36]. However, no direct comparison has been made regarding CMAS corrosion of both materials under the same conditions. Hence, we also investigated CMAS corrosion of $Yb_2Si_2O_7$ at 1300 °C for 96 h using $33CaO–9MgO–13AlO_{1.5}–45SiO_2$ CMAS with a mass loading of 60 mg·cm^{-2}. Figure 16 shows SEM backscattered electron images of $(Lu_{0.2}Yb_{0.2}Er_{0.2}Y_{0.2}Gd_{0.2})PO_4$ and $Yb_2Si_2O_7$ pellet cross-sections after CMAS reaction. For the phosphate, all CMAS was still at the pellet surface, and there was no significant change in the shape or volume of the pellet. Note that the large chips and cracks of the pellet at the bottom of the pellet are most likely induced by mechanical polishing during sample preparation since little CMAS penetrates through the bulk samples because of the rapid formation of a dense interaction layer upon CMAS interaction. However, in the case of the disilicate, there was no CMAS remaining at the top of the pellet, indicating that all CMAS penetrated the pellet, resulting in severe swelling with large voids and blister crack formation, which likely increased the rate of CMAS penetration. Our results, which are based on a side-by-side comparison, clearly show that the multicomponent phosphates display superior CMAS corrosion compared with $Yb_2Si_2O_7$ when tested under the same conditions (1300 °C, 96 h).

3.3 CMAS exposure of multicomponent rare-earth phosphates at 1400 °C

Few studies have investigated the behavior of multicomponent phosphates at relatively high temperatures [21], as most $REPO_4$–CMAS interaction experiments have been performed at 1300 °C [17,18]. Bryce *et al.* [21] reported the mechanism change of $REPO_4$–CMAS reaction for $(Lu_{0.2}Yb_{0.2}Er_{0.2}Y_{0.2}Gd_{0.2})PO_4$ tested at 1400 °C for 5 h and 1500 °C for 5 h with $40CaO–5MgO–5AlO_{1.5}–50SiO_2$ CMAS. At higher temperatures, the viscosity of the CMAS decreases, and the molten CMAS penetrates through the reaction layer into the bulk material along the grain boundaries of the rare-earth phosphates.

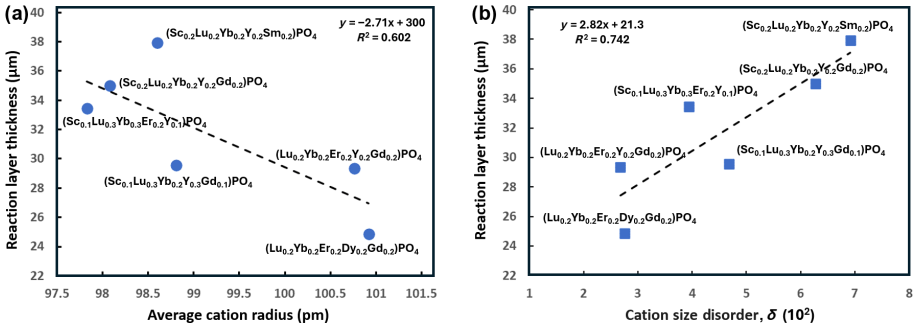

Fig. 15 Plots of measured reaction layer thickness of multicomponent phosphates after reaction with molten CMAS at 1300 °C for 96 h vs. (a) average ionic radii and (b) degree of cation size disorder.

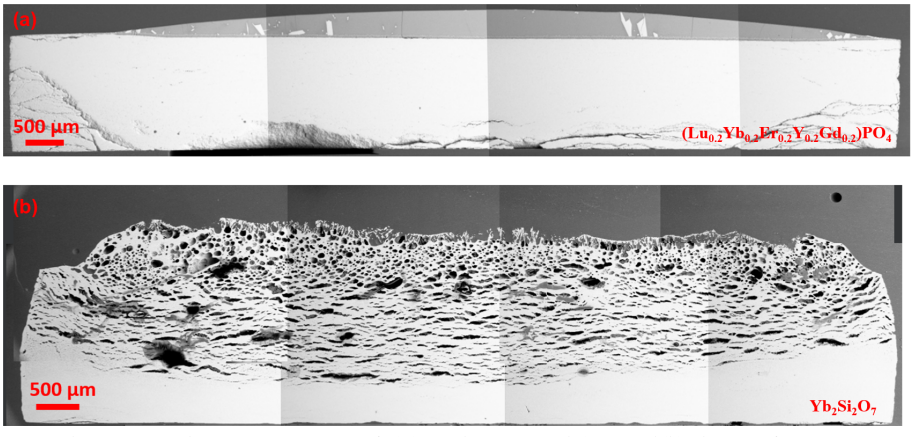

Fig. 16 Stitched backscattered SEM images showing cross-sections of (a) $(Lu_{0.2}Yb_{0.2}Er_{0.2}Y_{0.2}Gd_{0.2})PO_4$ and (b) $Yb_2Si_2O_7$ after CMAS exposure at 1300 °C for 96 h.

To further investigate high-temperature CMAS corrosion behavior and evaluate its performance against single-component phosphate, we also performed CMAS corrosion testing of $(Lu_{0.2}Yb_{0.2}Er_{0.2}Dy_{0.2}Gd_{0.2})PO_4$, $(Lu_{0.2}Yb_{0.2}Er_{0.2}Y_{0.2}Gd_{0.2})PO_4$, and $(Sc_{0.2}Lu_{0.2}Yb_{0.2}Y_{0.2}$-$Sm_{0.2})PO_4$ as well as the single-component $LuPO_4$ at 1400 °C for 5 h with $33CaO–9MgO–13AlO_{1.5}–45SiO_2$ CMAS. Figures S7–S10 in the ESM show XRD patterns taken at the surface layer of multicomponent rare earth phosphates and $LuPO_4$ pellets with CMAS deposits after heat treatment at 1400 °C for 5 h. The diffraction peaks for all 4 samples were indexed, and the bulk material $REPO_4$ along with $Ca_8MgRE(PO_4)_7$ phase was observed in all of XRD patterns, whereas an additional $Lu_2Si_2O_7$ phase was observed from $LuPO_4$–CMAS interaction. Bryce *et al.* [21] reported the formation of a cristobalite phase following the reaction between $(Lu_{0.2}Yb_{0.2}Er_{0.2}Y_{0.2}Gd_{0.2})PO_4$ and $40CaO–5MgO–5AlO_{1.5}–50SiO_2$ CMAS at 1400 °C for 5 h. However, this cristobalite phase was not observed in the present study, likely because of the relatively lower SiO_2 quantity in the residual CMAS.

SEM images at the interface of $LuPO_4$ pellet cross-section after CMAS reaction at 1400 °C for 5 h are displayed in Figs. 17(a) and 17(b). The cross-sectional images do not show the formation of a continuous reaction layer between the residual CMAS and the bulk pellet, and CMAS can be identified at the triple junctions of the bulk pellet grains (Fig. 17(b)), indicating the penetration of CMAS into the bulk pellet. Within the residual CMAS layer, large precipitates with a lighter contrast are observed, which are indexed as $Lu_2Si_2O_7$ on the basis of XRD analysis, whereas the smaller precipitates showing darker contrast are likely $Ca_8MgLu(PO_4)_7$. CMAS, however, does not penetrate the entirety of the pellet, nor is the penetration uniform, as CMAS is observed to penetrate deeper into the bulk pellet at some locations. Figures 17(c) and 17(d) show low- and high-magnification images at a location where CMAS has penetrated well below the surface of the bulk pellet, with Figs. 17(c) and 17(d) highlighting triple junctions with visible CMAS infiltration.

Figure 18 shows SEM backscattered electron images of $(Lu_{0.2}Yb_{0.2}Er_{0.2}Y_{0.2}Gd_{0.2})PO_4$–CMAS interface after the reaction at 1400 °C for 5 h. The reaction layer appears dense and forms along the entire length of CMAS–bulk pellet interface. The thickness is relatively uniform, approximately 23.8±7.2 μm, with no clear contrast variation. On the basis of XRD analysis, the reaction layer is confirmed to be $Ca_8MgRE(PO_4)_7$, and the precipitates within the residual CMAS with the same contrast are also likely to be the same $Ca_8MgRE(PO_4)_7$ phase. Similar to $LuPO_4$ sample, there is clear penetration of CMAS beyond the reaction layer, as evidenced by the darker contrast area (highlighted by the red dashed circles) observed between the grains of the bulk pellet below the reaction layer (Fig. 18(b)). Figures 18(c) and 18(d) show a clear infiltration front, where CMAS melt has penetrated below the reaction layer, with Fig. 18(d) clearly showing where CMAS penetration stopped (indicated by the red dashed line), as the darker contrast areas between the grains are no longer visible.

Figures 19(a) and 19(b) show SEM backscattered electron images of $(Lu_{0.2}Yb_{0.2}Er_{0.2}Dy_{0.2}Gd_{0.2})PO_4$–CMAS interface after the reaction at 1400 °C for 5 h. Similar to $(Lu_{0.2}Yb_{0.2}Er_{0.2}Y_{0.2}Gd_{0.2})PO_4$ sample, a dense continuous $Ca_8MgRE(PO_4)_7$ reaction layer formed between the bulk pellet and the residual CMAS, approximately 22.1±6.4 μm thick. $Ca_8MgRE(PO_4)_7$ precipitates also formed within the residual CMAS. There is clear penetration of CMAS below the reaction layer, as darker contrast CMAS is observed between the bulk pellet grains below the reaction layer. Figure 19(b) shows a high-magnification image taken at the bottom of the 1.76 mm thick pellet with visible CMAS between the grains.

Figures 20(a) and 20(b) show SEM backscattered electron

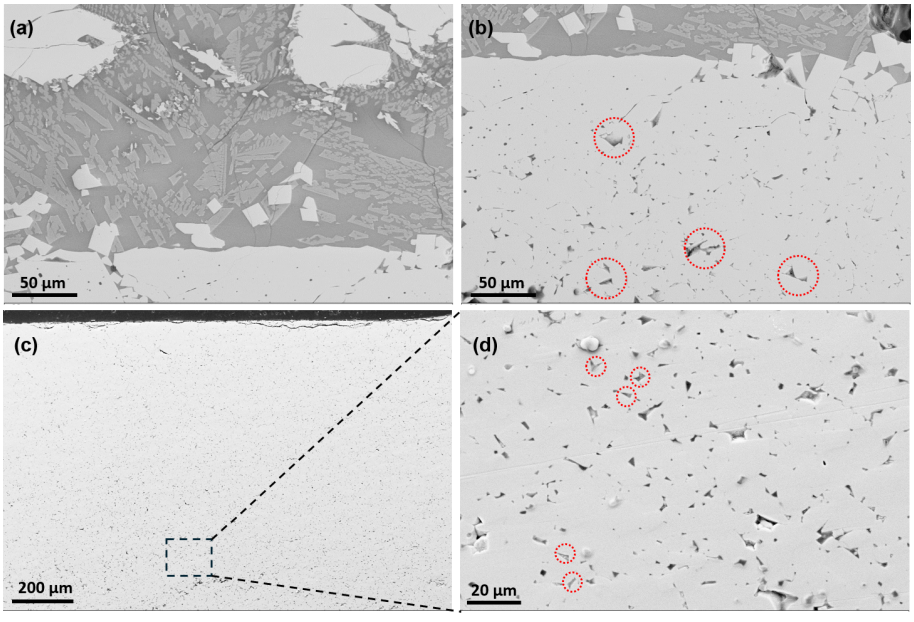

Fig. 17 SEM images of cross-sections of $LuPO_4$ interacting with molten CMAS at 1400 °C for 5 h. (a, b) Images of CMAS-bulk pellet reaction interface and (c) low- and (d) high-magnification images of CMAS penetrating bulk pellet. Red dashed circles indicate triple junctions where CMAS is observed.

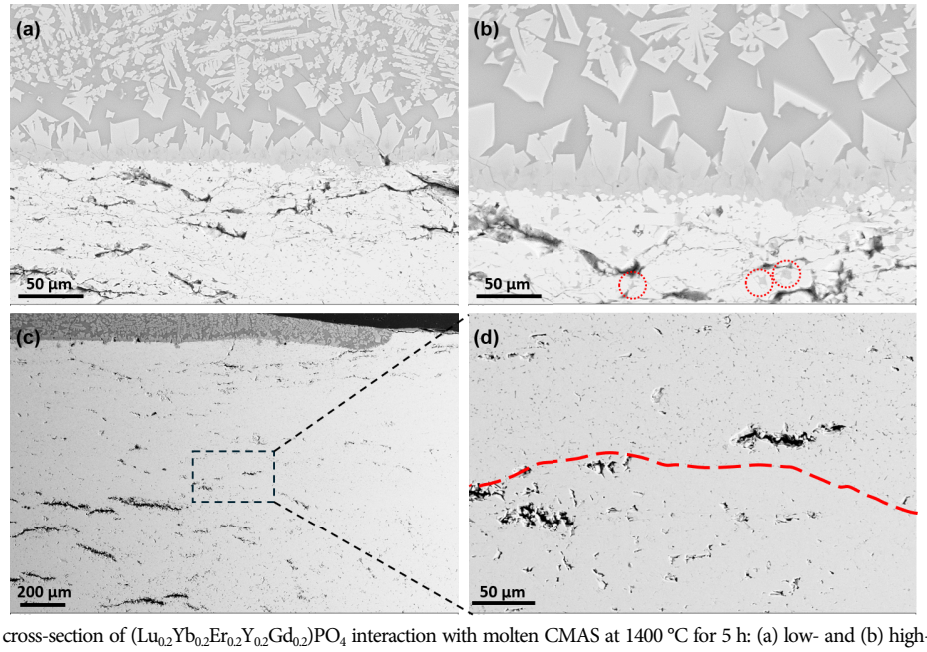

Fig. 18 SEM images of cross-section of $(Lu_{0.2}Yb_{0.2}Er_{0.2}Y_{0.2}Gd_{0.2})PO_4$ interaction with molten CMAS at 1400 °C for 5 h: (a) low- and (b) high-magnification images of reaction interface and (c) low- and (d) high-magnification images of CMAS penetrating bulk pellet. Red dashed circles indicate triple junctions where CMAS is observed.

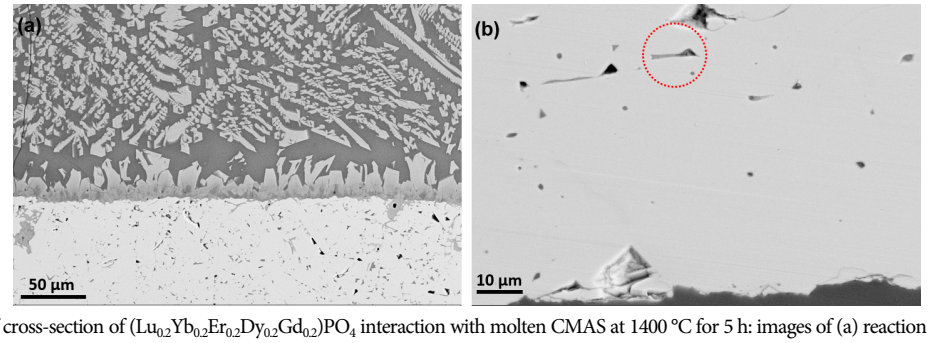

Fig. 19 SEM images of cross-section of $(Lu_{0.2}Yb_{0.2}Er_{0.2}Dy_{0.2}Gd_{0.2})PO_4$ interaction with molten CMAS at 1400 °C for 5 h: images of (a) reaction interface and (b) bottom of pellet.

images of $(Sc_{0.2}Lu_{0.2}Yb_{0.2}Y_{0.2}Sm_{0.2})PO_4$–CMAS reaction at 1400 °C for 5 h. Figure 20(a) shows the top surface where no residual CMAS or reaction layer is observed, and there is clear penetration of CMAS between the pellet grains accompanied by large voids

and cracks within the bulk material. Figure 20(b) shows an image taken at the bottom of the pellet where CMAS is visibly observed between the pellet grains, indicating complete penetration of CMAS throughout the entirety of the 1.9 mm thick pellet.

Clearly, there is a distinct change in the reaction mechanism from 1300 to 1400 °C. In the case of $LuPO_4$ and $(Sc_{0.2}Lu_{0.2}Yb_{0.2}Y_{0.2}Sm_{0.2})PO_4$, after CMAS corrosion at 1400 °C, no reaction layer is observed for either sample. However, $LuPO_4$ still has a significant amount of residual CMAS at the pellet surface, with CMAS only reaching between 200 and 800 μm below the pellet surface. However, no residual CMAS is observed at the top of $(Sc_{0.2}Lu_{0.2}Yb_{0.2}Y_{0.2}Sm_{0.2})PO_4$ pellet and CMAS infiltrates the entirety of the pellet, with large cracks and voids being formed due to the build-up of internal stress. Both $(Lu_{0.2}Yb_{0.2}Er_{0.2}Y_{0.2}Gd_{0.2})PO_4$ and $(Lu_{0.2}Yb_{0.2}Er_{0.2}Dy_{0.2}Gd_{0.2})PO_4$ form a dense and continuous $Ca_8MgRE(PO_4)_7$ reaction layer, but CMAS clearly penetrates the reaction layers. In the case of $(Lu_{0.2}Yb_{0.2}Er_{0.2}Dy_{0.2}Gd_{0.2})PO_4$, the reaction layer is slightly thinner, but CMAS appears to have penetrated deeper into the pellet, as CMAS is observed between the grains at the bottom of the pellet. Hence, the reaction layer thickness is not a particularly useful indicator of performance under these conditions.

Hu *et al.* [17] used the residual CMAS thickness as an indicator of the performance of rare earth phosphates under CMAS corrosion, but this thickness is specific to a particular CMAS loading. The formation of large voids within the residual CMAS, as shown in Fig. 21(a), could make the comparison of such measurements inaccurate. CMAS infiltration depth has also been used to compare the performance of different coating materials [44]. However, $(Lu_{0.2}Yb_{0.2}Er_{0.2}Dy_{0.2}Gd_{0.2})PO_4$ and $(Sc_{0.2}Lu_{0.2}Yb_{0.2}Y_{0.2}Sm_{0.2})PO_4$ samples show full infiltration of CMAS, whereas in $LuPO_4$ and $(Lu_{0.2}Yb_{0.2}Er_{0.2}Y_{0.2}Gd_{0.2})PO_4$), CMAS infiltration depths vary between 200–800 and 300–900 μm at different locations across the pellet cross section [44]. The recession depth of the bulk material may be a better factor for comparison, as it is directly related to the quantity of the bulk material consumed by CMAS melt. Figures 21(a)–21(d) show the pellet cross sections of $LuPO_4$, $(Lu_{0.2}Yb_{0.2}Er_{0.2}Y_{0.2}Gd_{0.2})PO_4$, $(Lu_{0.2}Yb_{0.2}Er_{0.2}Dy_{0.2}Gd_{0.2})PO_4$, and $(Sc_{0.2}Lu_{0.2}Yb_{0.2}Y_{0.2}Sm_{0.2})PO_4$ samples following CMAS reaction at 1400 °C for 5 h, where the measured recession depths are indicated. $LuPO_4$ has the largest recession depth of 72.7 μm, as it is more reactive with CMAS melt than $(Lu_{0.2}Yb_{0.2}Er_{0.2}Y_{0.2}Gd_{0.2})PO_4$ and $(Lu_{0.2}Yb_{0.2}Er_{0.2}Dy_{0.2}Gd_{0.2})PO_4$ samples, which have recession depths of 49.8 and 43.6 μm, respectively. The recession depth of $(Sc_{0.2}Lu_{0.2}Yb_{0.2}Y_{0.2}Sm_{0.2})PO_4$ sample could not be accurately measured. This comparison clearly indicates that $(Lu_{0.2}Yb_{0.2}Er_{0.2}Y_{0.2}Gd_{0.2})PO_4$ and $(Lu_{0.2}Yb_{0.2}Er_{0.2}Y_{0.2}Gd_{0.2})PO_4$ show improved resistance against CMAS corrosion relative to the single component $LuPO_4$, and the multicomponent compositions containing Sc have inferior CMAS corrosion resistance at higher temperatures.

In comparison, the reaction mechanisms for $REPO_4$–CMAS at 1300 and 1400 °C are relatively similar, where there is an initial dissolution of $REPO_4$ into CMAS melt followed by reprecipitation of $Ca_8MgRE(PO_4)_7$ phase between the bulk pellet and the interface. However, at 1300 °C, $Ca_8MgRE(PO_4)_7$ phase acts as a barrier between the bulk pellet and CMAS and reduces their interaction, whereas at 1400 °C, the viscosity of CMAS melt is reduced, and it more easily bypasses $Ca_8MgRE(PO_4)_7$ phase and infiltrates the bulk pellet via the grain boundaries, making CMAS dissolution along the grain boundaries the primary failure mode at 1400 °C.

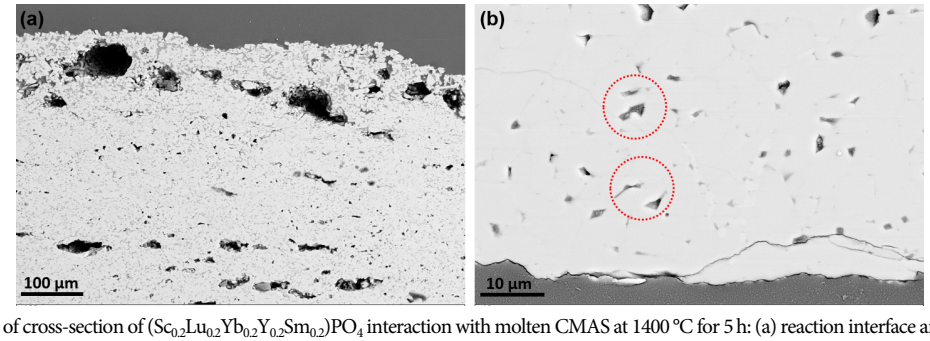

Fig. 20 SEM images of cross-section of $(Sc_{0.2}Lu_{0.2}Yb_{0.2}Y_{0.2}Sm_{0.2})PO_4$ interaction with molten CMAS at 1400 °C for 5 h: (a) reaction interface and (b) bottom of pellet.

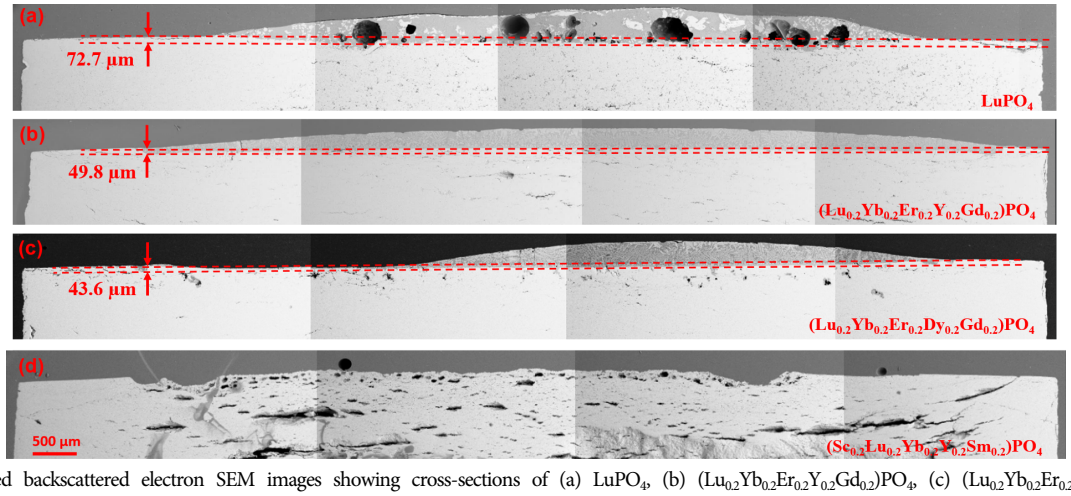

Fig. 21 Stitched backscattered electron SEM images showing cross-sections of (a) $LuPO_4$, (b) $(Lu_{0.2}Yb_{0.2}Er_{0.2}Y_{0.2}Gd_{0.2})PO_4$, (c) $(Lu_{0.2}Yb_{0.2}Er_{0.2}Dy_{0.2}Gd_{0.2})PO_4$, and (d) $(Sc_{0.2}Lu_{0.2}Yb_{0.2}Y_{0.2}Sm_{0.2})PO_4$ after CMAS exposure at 1400 °C for 5 h. Red dashed lines indicate height difference between original pellet surface and recessed surface.

CMAS corrosion experiments performed thus far have focused on understanding the reaction mechanism between the multicomponent phosphates and CMAS melt. Hence, bulk pellets have been tested with high CMAS mass loadings at long isothermal durations to facilitate as much of a reaction as possible between the two materials. The next stage of the experiments will investigate the performance of multicomponent rare earth phosphates as coatings on SiC substrates. To date, no studies have examined the microstructure of thermally sprayed rare earth phosphate coatings or the effects of increased porosity, cracks, defects, and splat boundaries on the thermal, mechanical, and chemical stability of these phosphates.

4 Conclusions

A systematic investigation of the thermomechanical properties and CMAS corrosion resistance of a series of multicomponent rare earth phosphates with a range of cation size disorders (2.68%–6.92%) was performed to evaluate their performance as potential EBC materials. The key material parameters governing their thermomechanical properties and optimized compositions with enhanced CMAS corrosion resistance were identified, guiding further development of multicomponent phosphates. All the multicomponent samples displayed lower thermal conductivity than the single-component rare earth phosphates did, and a strong negative correlation between the thermal conductivity of the multicomponent phosphates and the degree of cation disorder was identified. There is no direct correlation between CTE and the degree of cation size disorder or the average ionic radius. However, Er-containing multicomponent phosphates, such as $(Lu_{0.2}Yb_{0.2}Er_{0.2}Y_{0.2}Gd_{0.2})PO_4$ and $(Sc_{0.1}Lu_{0.3}Yb_{0.3}Er_{0.2}Y_{0.1})PO_4$, display the lowest CTEs over the range of 500–1573 K. In contrast, multicomponent phosphates containing smaller-sized Sc exhibit larger CTEs. The mechanical properties also showed no clear correlation with cation size disorder or the average ionic radius. Er-containing multicomponent phosphates displayed the highest fracture toughness at room temperature, whereas compositions with higher quantities of Sc presented the highest elastic modulus. $(Lu_{0.2}Yb_{0.2}Er_{0.2}Y_{0.2}Gd_{0.2})PO_4$ and $(Lu_{0.2}Yb_{0.2}Er_{0.2}Dy_{0.2}Gd_{0.2})PO_4$ display the thinnest reaction layer with continuous layer formation upon interaction with CMAS at 1300 °C for 96 h, indicating that they are the least reactive with CMAS melt. The incorporation of Sc into the multicomponent phosphate increases their reactivity with CMAS melt. At 1400 °C, $(Lu_{0.2}Yb_{0.2}Er_{0.2}Y_{0.2}Gd_{0.2})PO_4$ and $(Lu_{0.2}Yb_{0.2}Er_{0.2}Dy_{0.2}Gd_{0.2})PO_4$ samples show the least recession of their bulk material in the CMAS melt after 5 h. In general, multicomponent phosphates, e.g., $(Lu_{0.2}Yb_{0.2}Er_{0.2}Y_{0.2}Gd_{0.2})PO_4$, display enhanced CMAS corrosion resistance at high temperatures compared with single-component $LuPO_4$ and state-of-the-art disilicates. This is evidenced by the rapid formation of a dense and continuous interfacial layer, reduced reactivity, less CMAS penetration, and minimal recession of bulk materials without significant volumetric swelling. However, full CMAS infiltration of $(Lu_{0.2}Yb_{0.2}Er_{0.2}Dy_{0.2}Gd_{0.2})PO_4$ pellet is observed, whereas $LuPO_4$ and $(Lu_{0.2}Yb_{0.2}Er_{0.2}Y_{0.2}Gd_{0.2})PO_4$ only show partial infiltration of CMAS into their bulk pellets. These results highlight that despite the promising results of multicomponent phosphates for EBC applications, careful design of materials is necessary, e.g., with Er improving the fracture toughness and reducing the thermal expansion coefficient and without Sc to mitigate its potential detrimental effects on CMAS corrosion resistance.

Acknowledgements

This work was supported as part of the DMREF: Machine Learning Accelerated Design and Discovery of Rare-earth Phosphates as Next-Generation Environmental Barrier Coatings, a standard grant funded by the Division of Materials Research, National Science Foundation under Award DMREF-2119423.

Declaration of competing interest

The authors have no competing interests to declare that are relevant to the content of this article.

Electronic Supplementary Material

Supplementary material is available in the online version of this article at https://doi.org/10.26599/JAC.2024.9220978.

References

[1] Naslain R, Christin F. SiC-matrix composite materials for advanced jet engines. *MRS Bull* 2003, **28**: 654–658.

[2] Tejero-Martin D, Bennett C, Hussain T. A review on environmental barrier coatings: History, current state of the art and future developments. *J Eur Ceram Soc* 2021, **41**: 1747–1768.

[3] Liu JX, Shen XQ, Wu Y, *et al.* Mechanical properties of hot-pressed high-entropy diboride-based ceramics. *J Adv Ceram* 2020, **9**: 503–510.

[4] Toher C, Oses C, Esters M, *et al.* High-entropy ceramics: Propelling applications through disorder. *MRS Bull* 2022, **47**: 194–202.

[5] Sun J, Guo LX, Zhang YY, *et al.* Superior phase stability of high entropy oxide ceramic in a wide temperature range. *J Eur Ceram Soc* 2022, **42**: 5053–5064.

[6] Ye BL, Wen TQ, Chu YH. High-temperature oxidation behavior of $(Hf_{0.2}Zr_{0.2}Ta_{0.2}Nb_{0.2}Ti_{0.2})C$ high-entropy ceramics in air. *J Am Ceram Soc* 2020, **103**: 500–507.

[7] Fang GW, Gao XG, Song YD. A review on ceramic matrix composites and environmental barrier coatings for aero-engine: Material development and failure analysis. *Coatings* 2023, **13**: 357.

[8] Lee KN, Fox DS, Bansal NP. Rare earth silicate environmental barrier coatings for SiC/SiC composites and Si_3N_4 ceramics. *J Eur Ceram Soc* 2005, **25**: 1705–1715.

[9] Xiao GZ, Shen QY, Tian Y, *et al.* Investigation on the relation of microstructures and CMAS corrosion resistance of high entropy RE disilicates. *Corros Sci* 2024, **227**: 111727.

[10] Wei FS, Zhang DX, Gong X, *et al.* A systematic analysis of the calcium–magnesium–aluminosilicate corrosion behavior of high-entropy $(5Re_{0.2})_2Si_2O_7$ materials. *Corros Sci* 2023, **219**: 111221.

[11] Wang X, Cheng MH, Xiao GZ, *et al.* Preparation and corrosion resistance of high-entropy disilicate $(Y_{0.25}Yb_{0.25}Er_{0.25}Sc_{0.25})_2Si_2O_7$ ceramics. *Corros Sci* 2021, **192**: 109786.

[12] Abrar S, Ma Z, Liu L, *et al.* Excellent CMAS resistance of a newly developed equiatomic high entropy $(Dy_{1/4}Ho_{1/4}Tm_{1/4}Yb_{1/4})_2Si_2O_7$ ceramic pyrosilicate. *Ceram Int* 2023, **49**: 19840–19850.

[13] Wang X, Xu FH, Meng MY, *et al.* A new high entropy rare earth disilicate ceramic $(Lu_{1/8}Yb_{1/8}Sc_{1/8}Er_{1/8}Y_{1/8}Ho_{1/8}Dy_{1/8}Tb_{1/8})_2Si_2O_7$: High temperature corrosion of water vapor and molten calcium–magnesium–aluminosilicate (CMAS). *J Alloys Compd* 2024, **983**: 173687.

[14] Fan D, Zhong X, Zhang ZZ, *et al.* Interaction of high-entropy rare-earth monosilicate environmental barrier coatings subjected to corrosion by calcium–magnesium–alumino–silicate melts. *Corros Sci* 2022, **207**: 110564.

[15] Ren XM, Tian ZL, Zhang J, *et al.* Equiatomic quaternary $(Y_{1/4}Ho_{1/4}Er_{1/4}Yb_{1/4})_2SiO_5$ silicate: A perspective multifunctional thermal and environmental barrier coating material. *Scripta Mater* 2019, **168**: 47–50.

[16] Zhao ZF, Chen H, Xiang HM, *et al.* High-entropy $(Y_{0.2}Nd_{0.2}Sm_{0.2}Eu_{0.2}Er_{0.2})AlO_3$: A promising thermal/environmental barrier material for oxide/oxide composites. *J Mater Sci Technol* 2020, **47**: 45–51.

[17] Hu XX, Xu FF, Li KW, *et al.* Thermal properties and calcium–magnesium–alumina–silicate (CMAS) resistance of $LuPO_4$

as environmental barrier coatings. *J Eur Ceram Soc* 2020, **40**: 1471–1477.
[18] Ridley M, McFarland B, Miller C, *et al.* $YbPO_4$: A novel environmental barrier coating candidate with superior thermochemical stability. *Materialia* 2022, **21**: 101289.
[19] Zhang PX, Wang EH, Guo CY, *et al.* High-entropy rare earth phosphates ($REPO_4$, RE = Ho, Tm, Yb, Lu, Dy, Er and Y) with excellent comprehensive properties. *J Eur Ceram Soc* 2024, **44**: 1873–1879.
[20] Zhang PX, Duan XJ, Xie XC, *et al.* Xenotime-type high-entropy $(Dy_{1/7}Ho_{1/7}Er_{1/7}Tm_{1/7}Yb_{1/7}Lu_{1/7}Y_{1/7})PO_4$: A promising thermal/environmental barrier coating material for SiC_f/SiC ceramic matrix composites. *J Adv Ceram* 2023, **12**: 1033–1045.
[21] Bryce K, Shih YT, Huang LP, *et al.* Calcium–magnesium–aluminosilicate (CMAS) corrosion resistance of high entropy rare-earth phosphate $(Lu_{0.2}Yb_{0.2}Er_{0.2}Y_{0.2}Gd_{0.2})PO_4$: A novel environmental barrier coating candidate. *J Eur Ceram Soc* 2023, **43**: 6461–6472.
[22] Zhao ZF, Chen H, Xiang HM, *et al.* $(La_{0.2}Ce_{0.2}Nd_{0.2}Sm_{0.2}Eu_{0.2})PO_4$: A high-entropy rare-earth phosphate monazite ceramic with low thermal conductivity and good compatibility with Al_2O_3. *J Mater Sci Technol* 2019, **35**: 2892–2896.
[23] Zhang PX, Wang EH, Duan XJ, *et al.* Preparation and characterization of a novel monazite-type high-entropy $(La_{1/7}Ce_{1/7}Pr_{1/7}Nd_{1/7}Sm_{1/7}Eu_{1/7}Gd_{1/7})PO_4$ for thermal/environmental barrier coatings. *J Alloys Compd* 2023, **952**: 169978.
[24] Wright AJ, Wang QY, Ko ST, *et al.* Size disorder as a descriptor for predicting reduced thermal conductivity in medium- and high-entropy pyrochlore oxides. *Scripta Mater* 2020, **181**: 76–81.
[25] Nikiforova GE, Ryumin MA, Gavrichev KS, *et al.* High-temperature thermodynamic properties of $LuPO_4$. *Inorg Mater+* 2012, **48**: 841–844.
[26] Gavrichev KS, Ryumin MA, Tyurin AV, *et al.* Heat capacity and thermodynamic functions of $YbPO_4$ from 0 to 1800 K. *Inorg Mater+* 2013, **49**: 701–708.
[27] Gavrichev KS, Ryumin MA, Tyurin AV, *et al.* Thermodynamic functions of erbium orthophosphate $ErPO_4$ in the temperature range of 0–1600K. *Thermochim Acta* 2012, **535**: 1–7.
[28] Gavrichev KS, Ryumin MA, Tyurin AV, *et al.* Heat capacity and thermodynamic functions of xenotime YPO_4(c) at 0–1600 K. *Geochem Int+* 2010, **48**: 932–939.
[29] Gurevich VM, Ryumin MA, Tyurin AV, *et al.* Heat capacity and thermodynamic properties of $GdPO_4$ in the temperature range 0–1600 K. *Geochem Int+* 2012, **50**: 702–710.
[30] Rice RW. *Porosity of Ceramics*. Boca Raton (USA): CRC Press, 1998.
[31] Webster RI, Opila EJ. Mixed phase ytterbium silicate environmental-barrier coating materials for improved calcium–magnesium–alumino-silicate resistance. *J Mater Res* 2020, **35**: 2358–2372.
[32] Poerschke DL, Seward GGE, Levi CG. Influence of Yb : Hf ratio on ytterbium hafnate/molten silicate (CMAS) reactivity. *J Am Ceram Soc* 2016, **99**: 651–659.
[33] Yang K, Bryce K, Zhu WG, *et al.* Multicomponent pyrochlore solid solutions with uranium incorporation—A new perspective of materials design for nuclear applications. *J Eur Ceram Soc* 2021, **41**: 2870–2882.
[34] Almadhoni K, Khan S. Thermophysical properties of cellular aluminum and ceramic particulate/aluminum composites. *IJERA* 2015, **5**: 17–27.
[35] Kraftmakher Y. Equilibrium vacancies and thermophysical properties of metals. *Phys Rep* 1998, **299**: 79–188.
[36] Han J, Wang YF, Liu RJ, *et al.* Theoretical and experimental investigation of Xenotime-type rare earth phosphate $REPO_4$, (RE = Lu, Yb, Er, Y and Sc) for potential environmental barrier coating applications. *Sci Rep* 2020, **10**: 13681.
[37] Tian ZL, Zheng LY, Wang JM, *et al.* Damage tolerance and extensive plastic deformation of β-$Yb_2Si_2O_7$ from room to high temperatures. *J Am Ceram Soc* 2015, **98**: 2843–2851.
[38] Lawn BR. *Fracture of Brittle Solids*. Cambridge (UK): Cambridge University Press, 1993.
[39] Sun LC, Ren XM, Luo YX, *et al.* Exploration of the mechanism of enhanced CMAS corrosion resistance at 1500 °C for multicomponent $(Er_{0.25}Tm_{0.25}Yb_{0.25}Lu_{0.25})_2Si_2O_7$ disilicate. *Corros Sci* 2022, **203**: 110343.
[40] Tian ZL, Zhang J, Zheng LY, *et al.* General trend on the phase stability and corrosion resistance of rare earth monosilicates to molten calcium–magnesium–aluminosilicate at 1300 °C. *Corros Sci* 2019, **148**: 281–292.
[41] Majee BP, Bryce K, Huang L, Lian J. CMAS corrosion resistance of rare earth phosphates at high temperatures for environmental barrier coatings. *J Am Ceram Soc* 2024: e20251.
[42] Abrar S, Nazeer F, Ma Z, *et al.* Ultra-low thermal conductivity and hydrophobic properties of high entropy β-type quaternary pyrosilicate. *J Eur Ceram Soc* 2024, **44**: 1698–1709.
[43] Qian B, Wang Y, Zu JH, *et al.* A review on multicomponent rare earth silicate environmental barrier coatings. *J Mater Res Technol* 2024, **29**: 1231–1243.
[44] Kumar R, Rommel S, Jiang C, *et al.* Effect of CMAS viscosity on the infiltration depth in thermal barrier coatings of different microstructures. *Surf Coat Tech* 2022, **432**: 128039.